Article

Computational Modeling of Individual Red Blood Cell Dynamics Using Discrete Flow Composition and Adaptive Time-Stepping Strategies

Aymen Laadhari * and Ahmad Deeb

Department of Mathematics, College of Arts and Sciences, Khalifa University of Science and Technology, Abu Dhabi 127788, United Arab Emirates
*   Correspondence: aymen.laadhari@ku.ac.ae

Abstract: In this article, we present a finite element method for studying the dynamic behavior of deformable vesicles, which mimic red blood cells, in a non-Newtonian Casson fluid. The fluid membrane, represented by an implicit level-set function, adheres to the Canham–Helfrich model and maintains surface inextensibility constraint through penalty. We propose a two-step time integration scheme that incorporates higher-order accuracy by using an asymmetric composition of discrete flow based on the second-order backward difference formula, followed by a projection onto the real axis. Our framework incorporates variable time steps generated by an appropriate adaptation criterion. We validate our model through numerical simulations against existing experimental and numerical results in the case of purely Newtonian flow. Furthermore, we provide preliminary results demonstrating the influence of the non-Newtonian fluid model on membrane regimes.

Keywords: error estimation; composition method; numerical integration; high-order scheme; finite element method; red blood cell

1. Introduction

Red blood cells (RBCs) are the primary cellular component of blood flow and play a crucial role in delivering oxygen to the body. RBCs exhibit remarkable deformability, enabling them to traverse small capillaries without rupture under high hydrodynamic stress. The dynamics of RBCs and their interactions with other blood components give rise to non-Newtonian hemorheology, particularly in small vessels and damaged blood vessels [1]. While blood can be approximated as Newtonian in large arteries with high shear rates (that is, the shear stress is proportional to the shear rate) [2], it exhibits complex non-Newtonian characteristics (e.g., shear thinning, thixotropy, yield stress, etc.) in small-diameter arteries such as capillaries and tiny arterioles [3–6]. The intricate interactions of its cellular constituents lead to significant non-Newtonian differences in its hemorheological properties, which have been extensively studied experimentally and theoretically. At low shear rates, several experimental studies have been conducted, such as the one by Cokelet in 1963 [7]. Mathematical modeling of the spatio-temporal behavior of individual RBCs is an exciting and dynamic field of research. Through modeling, we aim to gain a better understanding of the complex patterns exhibited by RBCs at the microscopic scale. Despite significant progress, the behavior of RBCs remains non-trivial, and many challenges persist [8–10].

We focus on performing numerical simulations of a coupled system that models the interaction between an individual RBC's deformation and hydrodynamics using a realistic rheological model for blood at the RBC level. This modeling approach has significant importance and potential in several biomedical and therapeutic applications, such as the delivery of drugs, the treatment of cancer [11,12], and the production of biomolecules [13].

While there is growing interest in biomedical applications from the perspective of scientific computing and numerical modeling, most contributions in this field are focused on studying the dynamics of lipid vesicles in a purely Newtonian fluid. Vesicles are giant biomimetic unilamellar liposomes lacking a submembrane cytoskeleton and are commonly used as an instrumental model to study the behavior of RBCs in laboratory settings.

The mechanical properties of vesicles play a crucial role in their ability to withstand strong stresses and large deformations in flow, resulting in a wide variety of static and dynamic behaviors [14,15]. In the 1970s, Helfrich introduced a model for biomembranes where the mechanical properties are the result of bending energy minimization under constraints, also known as the Canham–Helfrich energy [16–18]. The bending energy density depends on the mean square curvature of the membrane. The bending force involves fourth-order derivative calculations of a shape function, which makes the problem numerically stiff and can result in several numerical difficulties [19–22].

In multiphysics modeling, there are two families of numerical strategies used for representing interfaces. Interface tracking techniques require moving meshes to track interface deformations, while interface capturing methods use fixed meshes and introduce an additional equation to implicitly track the interface [23].

The classical Galerkin finite element method [24], the boundary element method [25–27], the penalty-immersed boundary method [28], and the parametric finite element method [9,29] are examples of interface tracking techniques. On the other hand, the level-set method [22,30–34], the phase-field method [35,36], and the combined level-set and phase-field methods [37] are examples of interface capturing methods.

In this work, we use the level-set method because of the large deformations of the membrane. The level-set method has been proven effective for capturing the complex dynamics of interfaces with large deformations and topological changes [38–41].

At the microscopic scale, blood flow is characterized by the presence of aggregates of red blood cells that have a finite yield stress corresponding to a plastic solid behavior; it therefore cannot be modeled as a homogeneous Newtonian flow. Several studies have focused on the study of the non-Newtonian behavior of blood; see, for example, [42–45]. Numerous experimental studies have been performed on blood flow with different hematocrits, anticoagulants, and temperatures [46,47]. They have demonstrated that blood exhibits a finite yield strength in small vessels, owing to coagulation phenomena and the collective interactions of its components. To describe this behavior, Casson's model has proven effective in fine-tuning experimental measurements over a range of blood vessel diameters, hematocrit levels, and shear rates [48]. We also refer to the discussion on the choice of Casson's model for blood flow in [5]. Casson's model expresses shear stress with respect to shear rate and a minimum yield stress [49]; see Cokelet's work [7] for a comprehensive study. In this work, we have adopted the Casson constitutive model to describe the non-Newtonian behavior of blood at the RBC level.

As a result, blood behaves as an elastic solid at zero shear rate, when the shear stress decreases beneath the yield stress value. We often observe a change in behavior once the minimum yield limit of the fluid is exceeded [50]. However, dealing with the discontinuity of stress at a zero strain rate presents significant computational challenges. To address this challenge, various approaches have been introduced, with regularization techniques being a commonly used method. These techniques involve multiplying the stress by an exponential term [51–53] or simply regularizing the discontinuity at zero strain [54] in order to remove the singularity.

Given a system of differential equations obtained, for example, by finite element discretization, numerical integration using composition methods has emerged as a powerful tool for raising the order of a given lower-order basic integrator (i.e., first-order backward Euler scheme or second-order midpoint scheme) [55]. Here we introduce a technique for composing a second-order backward difference scheme, referred to as BDF-2, to increase the approximation order. This technique has been widely developed for one-step methods. For example, the Stromer–Verlet method [56], which is a symmetric and symplectic scheme

used in the simulation of the Hamiltonian system [57], is the result of the composition of two schemes with a half time step: the symplectic Euler scheme (also known as the Euler–Cromer rule) [58] and its adjoint (i.e., its inverse discrete flow using a negative time step). In general, for a numerical scheme and a given time step, the composition strategy is based on multiple composition of basic numerical flows using substeps of the original time step. A theoretical framework for composition methods applied to arbitrary symmetric basic integrators was developed [59]. Various works have been carried out to build a symmetric, symplectic [59], or pseudo-numerical flow from the composition of basic discrete flows [60,61] and to increase the order of the scheme [62]. Recently, complex coefficients have been used for the composition and construction of pseudo-symplectic and pseudo-symmetric flows [63]. In particular, a time-symmetric method corresponds to its own adjoint, which represents the inverse map of the original flow with opposite time step. Symmetric methods necessarily have even orders. The composition of multi-step methods into cyclic pathways [64] has been used to improve their stability domain. This technique has been applied to solve systems, such as in electromagnetics [65], in quantum mechanics for Klein–Gordon networks [66,67], in astronomy [68], in electric and chaotic systems [69], etc. We also refer the reader to [55,62,70,71].

Furthermore, adapted time-stepping strategies can be extremely useful to better follow the dynamics of highly deformable interfaces [72,73]. The adpted step sizes can be calculated if an appropriate local error estimate is available. This could be done by considering a composition method involving complex coefficients, so that the imaginary part of the output represents an error estimate of the numerical approximation. The strategy of taking into account complex coefficients in the composition technique has been used in [63] to produce pseudo-symmetric and symplectic schemes. Recently, an error estimation of the composed Cranck–Nikolson scheme has been proposed based on the imaginary part of the composed discrete flux using complex coefficients.

For multi-step methods, the technique is more technical. Multi-step composed methods in cyclic pathways were first developed in the 1980s to improve their stability domain [64]. In this work, we develop the composition technique of the BDF-2 scheme to increase the approximation order of integration in time. Indeed, the method consists of calculating, by using the last two approximations, an intermediate value by manipulating the coefficients associated with the BDF-2 scheme. This last intermediate value is then used with the last two solutions to predict an approximation such that the new coefficients verify third-order convergence conditions. This technique will allow us to adapt the time step based on the corresponding error estimate.

The paper is organized as follows. Section 2 presents the mathematical model and describes briefly the different subproblems for a vesicle immersed in a Casson fluid. Section 3 is devoted to the time discretization and the composition technique. The numerical method is presented in Section 4. In Section 5, several numerical simulations are provided in Newtonian and non-Newtonian cases, providing better information on the accuracy of the method. We close with some conclusions and possible extensions in Section 6.

2. Mathematical Framework

The spatio-temporal deformations of the vesicle are driven by the bending force, actions of fluid forces and boundary conditions, requiring the balance equations of mass and momentum. The fluid-membrane coupling is described through the balance of hydrodynamic stress by the bending response of the membrane. The level-set description of the membrane obeys a Hamilton–Jacobi equation.

2.1. Preliminaries

By $\Lambda \subset \mathbb{R}^2$, we denote a given open-bounded domain with polyhedral boundary $\partial \Lambda$ and denote by ν the outward unit normal vector on $\partial \Lambda$. Usual notation will be adopted for Lebesgue spaces $L^p(\Omega)$ and Sobolev spaces $H^s(\Omega)$ with norm $\|\cdot\|_{s,\Omega}$. For a time period $T > 0$ and for any time $t \in (0, T)$, let $\Gamma(t) = \partial \Omega(t)$ represent a vesicle immersed in the

domain Λ so that $\Gamma(t) \cap \partial\Lambda = \varnothing$; $\Omega(t)$ is the inner fluid domain, while $\Lambda \in \mathbb{R}^2$ is the exteracellular domain. In the following, the dependence of the shape on time is omitted to lighten the notations. Let **n** and H be the unit outward normal vector and mean curvature defined for Γ, respectively. See the schematic representation in Figure 1. As usual, I stands for the 2×2 identity tensor.
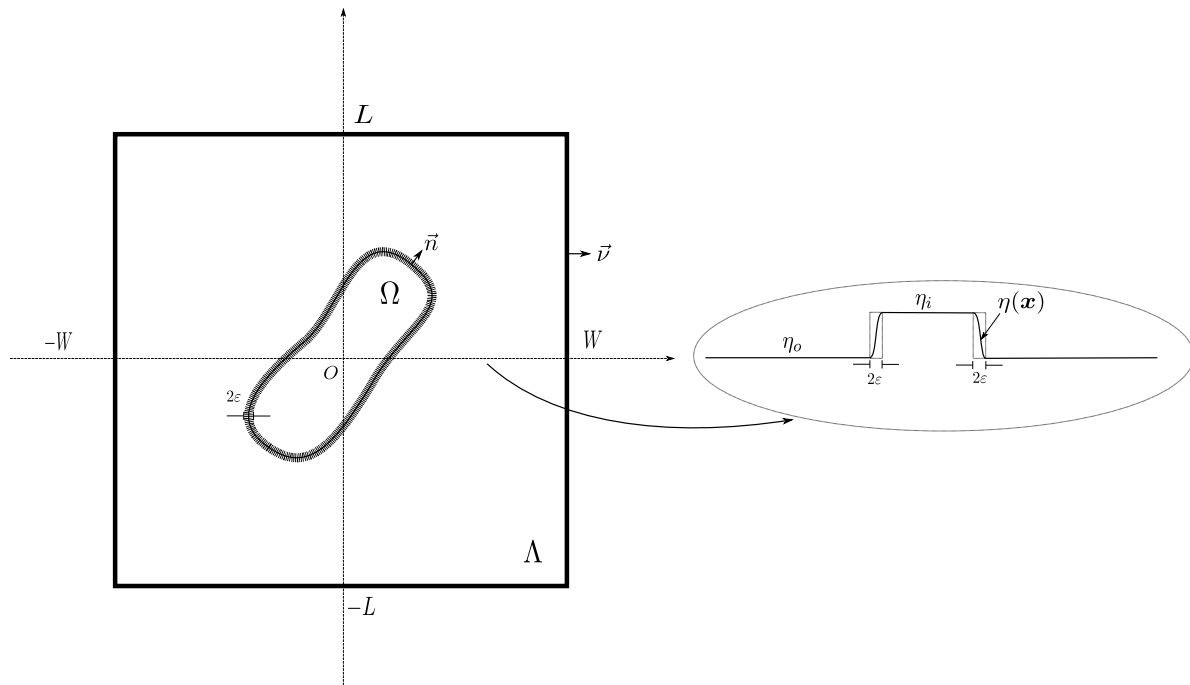
Figure 1. (**Left**) Simulation setup of a vesicle $\Gamma = \Gamma(t)$ with enclosed fluid domain $\Omega = \Omega(t)$ immersed in an incompressible non-Newtonian fluid domain $\Lambda \setminus \Omega(t)$ under simple shear flow conditions. A band of regularization along the circumference of the vesicle is of width 2ε. (**Right**) Cross-section of Γ representing a regularized sharp function η across the membrane.

2.2. Membrane Model

Consider a vesicle freely suspended in flow. It represents a two-dimensional inextensible fluidic membrane made of two monolayers of phospholipidic molecules. To describe the mechanical properties of lipid vesicles and also provide insight into the biconcave shapes of RBCs, Canham [17], Helfrich [16], and Evans [74] independently introduced a geometric model in the early 1970s, in which the mechanical response is driven by the minimization of a bending energy density dependent on the mean squared curvature. Given a geometrical form Ω in two-dimensional space, the energy functional is given by:

$$E(\Omega) = \frac{k}{2} \int_{\partial\Omega} H^2 \, ds, \tag{1}$$

where k is the bending rigidity modulus. The contribution of the Gaussian curvature is not relevant, if one is not interested in the change of topology; this is the case for RBCs.

We first adopt the limit of full incompressibility for both inner and outer fluids. In addition, the membrane is characterized by its local inextensibility, which forces the surface velocity divergence to vanish on the membrane. This allows it to resist stretching and leads to the preservation of the vesicle's perimeter (or area in 3D) [75].

From a numerical point of view, the local inextensibility is generally imposed by an exact local Lagrange multiplier acting as a position-dependent membrane tension [76] or by the minimization of an elastic energy, depending on the stretching [30]. The corresponding elastic force is strongly nonlinear, which can be a source of numerical instability. As a result, fluid incompressibility and membrane inextensibility result in the preservation of global

area and perimeter in 2D (or volume and surface in the 3D case). Let $\boldsymbol{u}$ be the fluid velocity. The inextensibility constraint reads:

$$div_s\,\boldsymbol{u} = 0, \quad (0,T) \times \Gamma, \tag{2}$$

where div_s is the surface divergence operator defined through the normal $\mathbf{n}$ on the membrane. Given the generic functions f and v, the surface gradient $\boldsymbol{\nabla}_s$, the surface divergence div_s, and the Laplace–Beltrami operators Δ_s, we write:

$$\begin{aligned}
\boldsymbol{\nabla}_s f &= (\boldsymbol{I} - \mathbf{n} \otimes \mathbf{n})\boldsymbol{\nabla} f, \\
div_s\,\boldsymbol{v} &= (\boldsymbol{I} - \mathbf{n} \otimes \mathbf{n}) : \boldsymbol{\nabla} v, \\
\Delta_s f &= div_s(\boldsymbol{\nabla}_s f).
\end{aligned}$$

Here, the crossed circle $\otimes$ represents the tensor product operator, while the semicolon : stands for the tensor contraction operator.

Based on shape optimization techniques [20], the bending force is given in the two-dimensional case by:

$$\boldsymbol{F} = k\left(\Delta_s H + \frac{H^3}{2}\right)\mathbf{n}, \quad \text{on } (0,T) \times \Gamma.$$

Considering the balance of surface forces and hydrodynamic stresses acting on the vesicle, the fluid/vesicle coupling is described by the jump of the normal Cauchy stress σ_{tot} [76]. The bending force is then transformed into a forcing surface term in the momentum equation:

$$[\![\sigma_{tot}\mathbf{n}]\!] = \boldsymbol{\nabla}_s \lambda - \lambda H\mathbf{n} + k\left(\Delta_s H + \frac{H^3}{2}\right)\mathbf{n} \quad \text{on } (0,T) \times \Gamma,$$

where λ stands for a local Lagrange multiplier associated with the inextensibility constraint (2).

2.3. Interface Tracking: Level-Set Representation

We use a level-set representation to follow the deformations of the vesicle $\Gamma(t)$, described in an implicit way as a zero level-set of a function φ:

$$\Gamma(t) = \left\{\boldsymbol{x} \in \Lambda;\ \varphi(t,\boldsymbol{x}) = 0\right\}. \tag{3}$$

The function φ is initialized with a signed distance $\varphi_0(\boldsymbol{x})$:

$$\varphi_0(\boldsymbol{x}) = \begin{cases} \displaystyle\inf_{\boldsymbol{y}\in\Gamma(0)} \|\boldsymbol{y} - \boldsymbol{x}\|, & \text{if } \boldsymbol{x} \notin \Omega(0) \\ -\displaystyle\inf_{\boldsymbol{y}\in\Gamma(0)} \|\boldsymbol{y} - \boldsymbol{x}\|, & \text{otherwise.} \end{cases}$$

All geometric fields are written in terms of φ and are extended to the entire domain Λ. In particular, $\mathbf{n} = \boldsymbol{\nabla}\varphi/|\boldsymbol{\nabla}\varphi|$ and $H = \text{div}\,\mathbf{n}$. The property of signed distance is lost by advection. To restitute the signed distance property, which is important for avoiding numerical instabilities resulting from very small or very high level-set gradients, a redistancing problem is commonly solved on a regular basis.

Surface integrals over Γ are approximated as integrals over Λ. Set a small regularization parameter $\varepsilon > 0$ proportional to the mesh size. We introduce regularized Heaviside $\mathcal{H}_\varepsilon$ and Dirac δ_ε functions as follows:

$$\mathcal{H}_\varepsilon(\varphi) = \begin{cases} 0, & \text{if } \varphi < -\varepsilon \\ \dfrac{1}{2}\left(1 + \dfrac{\varphi}{\varepsilon} + \dfrac{\sin\left(\dfrac{\pi\varphi}{\varepsilon}\right)}{\pi}\right), & \text{if } |\varphi| \leqslant \varepsilon \\ 1, & \text{otherwise} \end{cases},$$

$$\delta_\varepsilon(\varphi) = \dfrac{\mathrm{d}\mathcal{H}_\varepsilon}{\mathrm{d}\varphi}(\varphi) = \begin{cases} \dfrac{1}{2\varepsilon}\left(1 + \cos\left(\dfrac{\pi\varphi}{\varepsilon}\right)\right), & \text{if } |\varphi| \leqslant \varepsilon \\ 0, & \text{otherwise} \end{cases}.$$

For a function f and its extension $\tilde{f}$ on Λ, surface integrals are approximated as follows:

$$\int_\Gamma f(x)\, ds \approx \int_\Lambda |\boldsymbol{\nabla}\varphi|\, \delta_\varepsilon(\varphi)\, \tilde{f}(x)\, \mathrm{d}x. \tag{4}$$

The membrane force requires an evaluation of the fourth-order derivative of φ, which leads to a stiff problem with strong restrictions on the time step required for stability [33,76].

2.4. Non-Newtonian Fluid Model

Let $\boldsymbol{u}$ and p be the fluid velocity and pressure, respectively. Let $|\boldsymbol{\tau}| = \left(\frac{1}{2}\boldsymbol{\tau} : \boldsymbol{\tau}\right)^{1/2}$, with $\boldsymbol{\tau} \in \mathbb{R}^{2\times 2}$ denoting the Euclidean norms of tensors. Let the positive constant σ_0 be the yield stress. The membrane is suspended in an incompressible non-Newtonian fluid, where the constitutive law is given by the Casson model and expresses the Cauchy stress tensor σ_{tot} with respect to the the symmetric part of the velocity gradient (rate of deformation),

$$\mathbf{D}(\mathbf{u}) = \frac{1}{2}\left(\boldsymbol{\nabla}\boldsymbol{u} + \boldsymbol{\nabla}\boldsymbol{u}^T\right),$$

as follows:

$$\sigma_{tot} = \sigma - p\mathbf{I}.$$

Here, σ stands for the stress deviator tensor. Let $\eta(.)$ be the non-Newtonian viscosity function:

$$\begin{cases} \sigma = 2\eta(|\mathbf{D}(\mathbf{u})|)\mathbf{D}(\mathbf{u}) = \left(\sqrt{K} + \sqrt{\dfrac{\sigma_0}{|\mathbf{D}(\boldsymbol{u})|}}\right)^2 \mathbf{D}(\boldsymbol{u}), & \text{when } |\mathbf{D}(\boldsymbol{u})| \neq 0, \\ |\sigma| < \sigma_0, & \text{when } |\mathbf{D}(\boldsymbol{u})| = 0, \end{cases}. \tag{5}$$

Here, Casson's viscosity constant K corresponds to the fluid viscosity in the Newtonian case, that is, when the yield stress equals zero. Indeed, $\sigma_0 = 0$ reduces the constitutive equation to the Navier–Stokes case with a symmetric Cauchy stress and proportionality constant given by the constant K. Note that the stress is undetermined when $\mathbf{D}(\boldsymbol{u}) = \mathbf{0}$, while we only know that it is less than the yield stress value. The viscosity function decreases as the shear rate increases.

According to [50], the reported yield stress values vary between 0.0002 and 0.04 Pa, while the Casson viscosity constant is $K \approx 0.56$ Pa·s [77]. The relation (5) is not defined when the shear rate vanishes, and one proceeds by regularization with a small positive parameter ξ. The limiting case $\xi \to 0$ allows us to retrieve Casson's original model; see, for example, [52,78]. By analogy with the Newtonian case, we consider different Casson's viscosity constants of the internal and external fluids, referred to as K_i and K_o, respectively. Accordingly, the problem is modified in order to go back to standard equations, where the fluid behaves as a quasi-Newtonian fluid. That allows the use of standard solvers. The deviator stress in (5) writes:

$$\sigma = 2\eta^*(|\mathbf{D}(\mathbf{u})|)\mathbf{D}(\mathbf{u}),$$

with a viscosity function:

$$
\eta^*(\mathbf{D}(\boldsymbol{u})) =
\begin{cases}
\dfrac{1}{2}\left(\sqrt{K_i} + \sqrt{\dfrac{\sigma_0}{|\mathbf{D}(\boldsymbol{u})| + \xi}}\right)^2, & \text{in } \Omega, \\[2.5ex]
\dfrac{1}{2}\left(\sqrt{K_o} + \sqrt{\dfrac{\sigma_0}{|\mathbf{D}(\boldsymbol{u})| + \xi}}\right)^2, & \text{otherwise}.
\end{cases}
\tag{6}
$$

To remedy the discontinuity of the viscosity accross the membrane in (6), the sharp viscosity is replaced by a smooth function:

$$
\eta_\varepsilon^*(\mathbf{D}(\boldsymbol{u}), \varphi) = \frac{1}{2}\left(\sqrt{K_o}\,\mathcal{H}_\varepsilon(\varphi) + \sqrt{K_i}(1 - \mathcal{H}_\varepsilon(\varphi)) + \sqrt{\frac{\sigma_0}{|\mathbf{D}(\boldsymbol{u})| + \xi}}\right)^2, \quad \text{in } \Lambda.
\tag{7}
$$

That results in a symmetric and regularized Cauchy stress tensor.

Dimensionless Nonlinear Coupled Problem

Assume a constant piecewise fluid density equal to ρ_i and ρ_o in the intracellular and extracellular domains, respectively. Consider a vesicle in simple shear flow as depicted in Figure 1. Opposite constant velocities $\boldsymbol{u} = (\pm V_b, 0)$ are imposed on the horizontal boundaries Σ_D, while stress-free boundary conditions are imposed elsewhere. Let Σ_- denote the inflow domain. Admissible velocities belong to:

$$
\mathbb{V}(V_b) = \left\{ \mathbf{v} \in \left(H^1(\Lambda)\right)^2 \text{ s.t. } \mathbf{v} = (V_b, 0)^T \text{ on } \Sigma_D \right\}.
$$

To write the dimensionless problem, we introduce some dimensionless parameters of hemodynamical relevance. Given φ_0, the vesicle initially has a perimeter of $|\Gamma(0)|$. Set $R_0 = |\Gamma(0)|/2\pi$ as the radius of a circle having the same circumference as the membrane. The confinement of the vesicle in Λ is denoted by the dimensionless parameter $\alpha = R_0/L$. To normalize the problem, we consider the characteristic length $\alpha_x = L/\alpha$, the characteristic velocity $\alpha_{\boldsymbol{u}} = \alpha V_b$, the characteristic time $\alpha_t = \alpha_x/\alpha_{\boldsymbol{u}}$, and the characteristic pressure $\alpha_p = R_0^2 K_0 V_v/L^3$. We choose ρ_o and K_o in the extracellular domain as characteristic density and viscosity, respectively.

We end up with a set of dimensionless physical parameters. The Reynolds number Re assesses inertial forces with respect to viscous forces. The bending capillary number Ca compares the force of the imposed flow to the membrane bending strength. Bingham's number measures the effect of the yield stress against the rate of fluid strain. The viscosity contrast $\beta = K_i/K_o$ compares the intracellular viscosity to the extracellular viscosity in the Newtonian case. The same is true for the density contrast ρ_i/ρ_o. Without loss of generality, we assume similar intra- and extracellular densities as usual $\rho_i/\rho_o \approx 1$, since this parameter is known not to have an effect on the vesicle dynamics. Finally, a parameter of great importance is the reduced area; it represents the deflation of the cell which is the ratio between the enclosed area and the area of a circle having the same perimeter. The dimensionless parameters of the problem are:

$$
\text{Re} = \frac{\rho_o L V_b}{K_o}, \qquad\qquad \text{Ca} = \frac{k\,K_o\,L^3\,V_b}{R_0}, \qquad \text{Bn} = \frac{\sigma_0 L^3}{K_o R_0^2 V_b},
$$

$$
\Xi_{2D} = \frac{|\Omega|}{\pi} \times \left(\frac{2\pi}{|\Gamma|}\right)^2, \qquad\qquad \alpha = \frac{R_o}{L}, \qquad\qquad \beta = \frac{K_i}{K_o}.
$$

We also refer to the work of Laadhari et al. [31,76] for a detailed description of the dimensionless problem and for obtaining the dimensionless physical parameters in the Newtonian case. In the following, all quantities are dimensionless, while the same previous notation is used. The regularization parameter is always denoted by ξ. The normalized problem is written as:

find φ, $\mathbf{u}$, p, and λ such that

$$\frac{\partial \varphi}{\partial t} + \mathbf{u}.\boldsymbol{\nabla}\varphi = 0 \text{ in } (0,T) \times \Lambda \tag{8a}$$

$$\text{Re}\left(\frac{\partial \mathbf{u}}{\partial t} + \mathbf{u}.\boldsymbol{\nabla}\mathbf{u}\right) - \mathbf{div}(2\eta_\varepsilon^*(\mathbf{D}(\mathbf{u}),\varphi)\mathbf{D}(\mathbf{u})) + \boldsymbol{\nabla}p = 0 \text{ in } (0,T) \times (\Lambda\backslash\Gamma) \tag{8b}$$

$$\text{div } \mathbf{u} = 0 \text{ in } (0,T) \times \Lambda \tag{8c}$$

$$\text{div}_s \mathbf{u} = 0 \text{ on } (0,T) \times \Gamma \tag{8d}$$

$$[\![\mathbf{u}]\!] = 0 \text{ on } (0,T) \times \Gamma \tag{8e}$$

$$-\frac{1}{\text{Ca}}\left\{\Delta_s H + \frac{H^3}{2}\right\}\mathbf{n}$$
$$+H\,\lambda\,\mathbf{n} - \boldsymbol{\nabla}_s\lambda + [\![2\eta_\varepsilon^*(\mathbf{D}(\mathbf{u}),\varphi)\mathbf{D}(\mathbf{u}) - p\mathbf{I}]\!].\mathbf{n} = 0 \text{ on } (0,T) \times \Gamma \tag{8f}$$

$$\varphi = \varphi_b \text{ on } (0,T) \times \Sigma_- \tag{8g}$$

$$\mathbf{u} = \mathbf{u}_b \text{ on } (0,T) \times \Sigma_D \tag{8h}$$

$$(2\eta_\varepsilon^*(\mathbf{D}(\mathbf{u}),\varphi)\mathbf{D}(\mathbf{u}) - p\mathbf{I}).\boldsymbol{\nu} = 0 \text{ on } (0,T) \times \partial\Lambda\backslash\Sigma_D \tag{8i}$$

$$\varphi(0) = \varphi_0 \text{ in } \Lambda \tag{8j}$$

$$\mathbf{u}(0) = \mathbf{u}_0 \text{ in } \Lambda. \tag{8k}$$

The normalized smooth viscosity function is:

$$\eta_\varepsilon^*(\mathbf{D}(\mathbf{u}),\varphi) = \frac{1}{2}\left(\mathcal{H}_\varepsilon(\varphi) + \sqrt{\beta}(1 - \mathcal{H}_\varepsilon(\varphi)) + \sqrt{\frac{\text{Bn}}{|\mathbf{D}(\mathbf{u})| + \xi}}\right)^2, \quad \text{in } \Lambda. \tag{9}$$

3. Composition Technique Applied to the Second-Order BDF Scheme

In this section, we focus on the construction of a higher-order scheme by double composition of the second-order BDF scheme. Let us simply note the differential system obtained by finite element discretization by the following initial value problem:

$$\frac{dy}{dt} = f(t,y), \quad y(0) = y_0, \quad t \geqslant 0. \tag{10}$$

For time interval $[0,T]$, we consider a partition into N sub-intervals $[t_n, t_{n+1})$, $n = 0,\ldots,N-1$ of step size Δt. For all $n \geqslant 1$, the unknowns y_n approach the true solution $y(t)$ at discrete time steps t_n and are calculated by induction. Given a numerical scheme and $n \geqslant 1$, let Y be the numerical flow such that:

$$y_n = Y_{\Delta t}(y_{n-1}), \quad \text{and} \quad \underbrace{Y_{\Delta t} \circ \ldots \circ Y_{\Delta t}(y_0)}_{n \text{ times}} = y_n.$$

The numerical scheme is of order p if $y(t_n) - Y_{\Delta t}(y_{n-1}) = \mathcal{O}(\Delta t^{p+1})$. Given a basic integrator with a low order p, composition methods allow us to raise the order of the scheme by constructing a composed numerical flow $Y_{a_1\Delta t} \circ \cdots \circ Y_{a_s\Delta t}$, composing the basic one s times. According to [55] (Theorem 4.1, Section II.4), the composed flow is at least of order $p+1$ if and only if the coefficients $a_1,\ldots,a_s$ verify the conditions $a_1 + \ldots + a_s = 1$ and $a_1^{p+1} + \cdots + a_s^{p+1} = 0$. For all s, these two algebraic equations have no real solution if p is odd. To construct symmetric schemes with even orders, it has been suggested to start with a second-order integrator and consider a three-times symmetric composition (i.e., $s = 3$ and $a_3 = a_1$) to produce the so-called triple-jump numerical flow; see, e.g., [55] (page 44) and [79]. In fact, this results from considering only symmetric compositions of second-order integrators, i.e., methods with weighting coefficients satisfying an additional condition $a_{s+1-i} = a_i$ with $i = 1, \cdots, s$. This composition has $a_2 < 0$, which limits its

application for any non-reversible vector field. For $s = 2$ and any order p, these algebraic equations have complex solutions:

$$a_1 = \frac{1}{2} + \frac{i}{2} \frac{\sin\left(\dfrac{\pi}{p+1}\right)}{1 + \cos\left(\dfrac{\pi}{p+1}\right)} \quad \text{and} \quad a_2 = \overline{a_1}, \tag{11}$$

leading to higher-order pseudo-symmetric and symplectic numerical flows [63].

Note that this technique and the choice of sub-step sizes (11) are valid for raising the orders of one-step methods, whereas this framework is not applicable to multi-step methods such as the BDF-2 method. In the following, we develop a procedure for a two-step asymmetric composition of the BDF-2 scheme using complex coefficients to both (i) increase the order of the time scheme, and also (ii) adapt the time step using the imaginary part of the compose numerical flow.

3.1. Second-Order Backward Differentiation BDF-2

For $n > 1$ and given y_{n-2} and y_{n-1}, a numerical approximation of $y(t_n)$ is computed using the BDF-2 scheme. For a constant time step Δt, the BDF-2 scheme applied to (10) approximates y_n as follows:

$$3y_n - 4y_{n-1} + y_{n-2} = 2\Delta t f(t_n, y_n).$$

For an adaptive time step Δt_n, the difference formula rather involves some coefficients γ_i, with $i = 0, 1, 2$; see, for example, [80] (Appendix G.7). The approximated solution verifies:

$$\gamma_2 y_n + \gamma_1 y_{n-1} + \gamma_0 y_{n-2} = \Delta t_n f(t_n, y_n), \quad \text{with } \Delta t_n = t_n - t_{n-1}.$$

This approximation can be seen as the output of the associated numerical flow, referred to as:

$$(y_n, y_{n-1}) = Y_{\Delta t_n, \gamma_i}^{\text{BDF}-2}(y_{n-1}, y_{n-2}).$$

In what follows, we develop a technique to increase the order of BDF-2 using the double composition of the same discrete flow $Y_{\Delta t_n, \gamma_i}^{\text{BDF}-2}$ with appropriate time step and scheme coefficients. To our knowledge, the developed approach is novel for the BDF-2 scheme, while we refer to [64,81,82] for more information on the composition of multi-step methods in a cyclic way.

The method is based on computing a first approximate solution after a first jump at time $t_{n-1/2}$ using a BDF-2 method and a correctly chosen complex substep size so that the solution y_n at time t_n is obtained by double composition of BDF-2. A schematic representation of the extension to the complex space and two-step solution is provided in Figure 2. It can be summarized as follows:

Step 1: $(y_{n-1/2}, y_{n-1}) = Y_{a_1 \Delta t_n, \gamma_i}^{\text{BDF2}}(y_{n-1}, y_{n-2})$,

Step 2: $(y_n, y_{n-1}) = \text{Re}\left(Y_{a_2 \Delta t_n, \omega_i}^{\text{BDF2}} \circ Y_{a_1 \Delta t_n, \gamma_i}^{\text{BDF2}}(y_{n-1}, y_{n-2}) \right)$,

where the parameters a_1, a_2, Δt_n, γ_i and ω_i will be explicitly introduced in the following subsections.
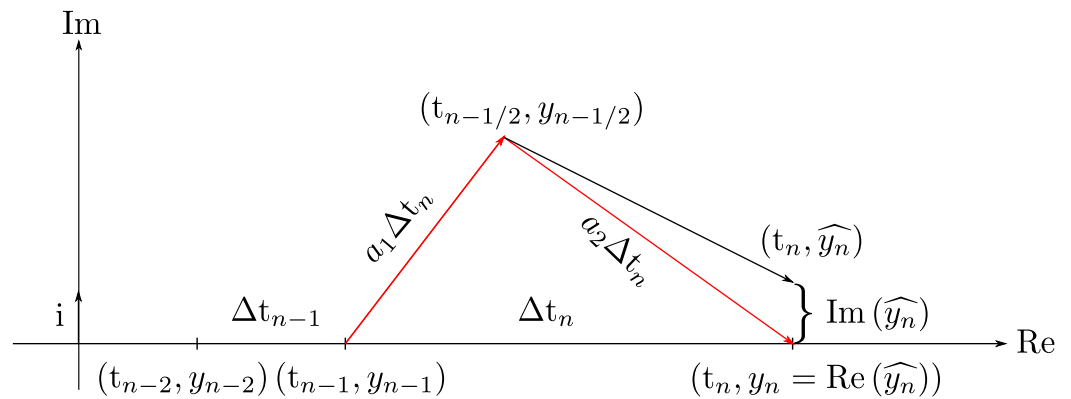
Figure 2. Schematic representation of the BDF-2 flow composition method and the entire solution method.

3.2. Step 1: Calculation of an Intermediate Solution

For all $n > 2$, consider the time steps Δt_n so that $t_n = t_{n-1} + \Delta t_n$. Our goal is to produce a third-order approximation of $y(t_n)$ using y_{n-2} and y_{n-1}. We first compute an intermediate step solution, denoted $y_{n-1/2}$, between y_{n-1} and the desired y_n using y_{n-2} and y_{n-1}. Thus, $y_{n-1/2} \approx y(t_{n-1/2})$ follows the BDF-2 scheme and is given by:

$$\gamma_2 y_{n-1/2} + \gamma_1 y_{n-1} + \gamma_0 y_{n-2} = (t_{n-1/2} - t_{n-1}) f(t_{n-1/2}, y_{n-1/2}), \tag{12}$$

where $t_{n-1/2} = t_{n-1} + a_1 \Delta t_n$, and a_1 is a substep coefficient to be set subsequently. The coefficients γ_0, γ_1, and γ_2 shall satisfy:

$$y(t_{n-1/2}) - y_{n-1/2} = \mathcal{O}\left((a_1 \Delta t_n)^3\right).$$

Note that, for a BDF scheme with a given order, the coefficients in both fixed and variable time steps do not depend obviously on the function f. We refer the interested readers to [72] (page 412, Equation (5.12)) for more details. We follow the procedure in [80] (Appendix G.7) to find the coefficients γ_i. Set $f(t, y) = y$, so that $y_0 e^t$ is a solution of (10). We express y_{n-2} and y_{n-1} in terms of $y_{n-1/2}$:

$$y_{n-2} = e^{-(t_{n-1/2} - t_{n-2})} y_{n-1/2} \quad \text{and} \quad y_{n-1} = e^{-(t_{n-1/2} - t_{n-1})} y_{n-1/2}.$$

By substituting in (12), we get:

$$\gamma_2 + \gamma_1 e^{-(t_{n-1/2} - t_{n-1})} + \gamma_0 e^{-(t_{n-1/2} - t_{n-2})} = t_{n-1/2} - t_{n-1}. \tag{13}$$

By performing Taylor series expansions in (13), we obtain:

$$\gamma_2 \quad + \gamma_1\left[1 - (t_{n-1/2} - t_{n-1}) + \tfrac{1}{2}(t_{n-1/2} - t_{n-1})^2 + \cdots\right]$$
$$+ \gamma_0\left[1 - (t_{n-1/2} - t_{n-2}) + \tfrac{1}{2}(t_{n-1/2} - t_{n-2})^2 + \cdots\right] = t_{n-1/2} - t_{n-1}.$$

Considering terms up to the second order gives the following linear system:

$$\begin{cases} \gamma_0 + \gamma_1 + \gamma_2 &= 0 \\ \varepsilon'_n \gamma_0 + \gamma_1 + 1 &= 0 \\ {\varepsilon'_n}^2 \gamma_0 + \gamma_1 &= 0 \end{cases}, \qquad \text{with} \quad \varepsilon'_n = \frac{t_{n-1/2} - t_{n-2}}{t_{n-1/2} - t_{n-1}}. \tag{14}$$

The solution for the above linear system is expressed by:

$$\gamma_0 = \frac{1}{\varepsilon'_n(\varepsilon'_n - 1)}, \quad \gamma_1 = -\frac{\varepsilon'_n}{\varepsilon'_n - 1} \quad \text{and} \quad \gamma_2 = \frac{\varepsilon'_n + 1}{\varepsilon'_n}. \tag{15}$$

As a consequence, $y_{n-1/2}$ is written as:

$$y_{n-1/2} = \frac{\gamma_0}{(t_{n-1/2} - t_{n-1}) - \gamma_2} y_{n-2} + \frac{\gamma_1}{(t_{n-1/2} - t_{n-1}) - \gamma_2} y_{n-1}. \tag{16}$$

Remark 1. *If the time steps are equally spaced, that is $\Delta t = t_{n-1} - t_{n-2} = t_{n-1/2} - t_{n-1}$, then $\varepsilon_n' = 2$, $\gamma_0 = 1/2$, $\gamma_1 = -4/2$, and $\gamma_2 = 3/2$. We recover the BDF-2 formula with fixed step size:*

$$3y_{n-1/2} - 4y_{n-1} + y_{n-2} = 2\Delta t \, f(t_{n-1/2}, y_{n-1/2}). \tag{17}$$

3.3. Step 2 and Solution Method

In the following, we use the three points y_{n-2}, y_{n-1}, and $y_{n-1/2}$ to calculate an approximation y_n of $y(t_n)$; see Figure 2. We define a suitable condition to eliminate y_{n-2}, thus using only y_{n-1} and $y_{n-1/2}$ and reducing Step 2 to a two-step method to calculate y_n. We seek y_n that satisfy the following third-order backward difference formula:

$$\omega_2 y_n + \omega_1 y_{n-1/2} + \omega_0 y_{n-1} + \omega_{-1} y_{n-2} = (t_n - t_{n-1/2}) f(t_n, y_n). \tag{18}$$

Similar to the previous subsection, we write y_{n-2}, y_{n-1} in terms of y_n and express $y_{n-1/2}$ using (16):

$$
\begin{aligned}
y_{n-2} &= e^{-(t_n - t_{n-2})} y_n, \\
y_{n-1} &= e^{-(t_n - t_{n-1})} y_n, \\
y_{n-1/2} &= \frac{\gamma_0 e^{-(t_n - t_{n-2})} + \gamma_1 e^{-(t_n - t_{n-1})}}{(t_{n-1/2} - t_{n-1}) - \gamma_2} y_n.
\end{aligned}
$$

By substituting in (18), we get:

$$\omega_2 + \omega_1 \frac{\gamma_0 e^{-(t_n - t_{n-2})} + \gamma_1 e^{-(t_n - t_{n-1})}}{(t_{n-1/2} - t_{n-1}) - \gamma_2} + \omega_0 e^{-(t_n - t_{n-1})} + \omega_{-1} e^{-(t_n - t_{n-2})} = (t_n - t_{n-1/2}).$$

By performing Taylor series expansions up to order 4, we obtain:

$$
\begin{aligned}
&\omega_{-1}\left((t_{n-1/2} - t_{n-1}) - \gamma_2 \right)\left[1 - (t_n - t_{n-2}) + \frac{1}{2}(t_n - t_{n-2})^2 - \frac{1}{6}(t_n - t_{n-2})^3 + \cdots \right] + \\
&\omega_0\left((t_{n-1/2} - t_{n-1}) - \gamma_2 \right)\left[1 - (t_n - t_{n-1}) + \frac{1}{2}(t_n - t_{n-1})^2 - \frac{1}{6}(t_n - t_{n-1})^3 + \cdots \right] + \\
&\omega_1 \gamma_0 \left[1 - (t_n - t_{n-2}) + \frac{1}{2}(t_n - t_{n-2})^2 - \frac{1}{6}(t_n - t_{n-2})^3 + \cdots \right] + \\
&\omega_1 \gamma_1 \left[1 - (t_n - t_{n-1}) + \frac{1}{2}(t_n - t_{n-1})^2 - \frac{1}{6}(t_n - t_{n-1})^3 + \cdots \right] + \\
&\omega_2\left((t_{n-1/2} - t_{n-1}) - \gamma_2 \right) = \left((t_{n-1/2} - t_{n-1}) - \gamma_2 \right)(t_n - t_{n-1/2}).
\end{aligned}
$$

The equation can be arranged as follows:

$$
\begin{aligned}
&-\omega_{-1}\gamma_2 - \omega_0\gamma_2 + \omega_1(\gamma_1 + \gamma_2) - \omega_2\gamma_2 \\
&+ (\omega_{-1} + \omega_0 + \omega_2)(t_{n-1/2} - t_{n-1}) + (\gamma_2\omega_{-1} - \omega_1\gamma_0)(t_n - t_{n-2}) + (\gamma_2\omega_0 - \gamma_1\omega_1)(t_n - t_{n-1}) \\
&- (\omega_{-1}(t_n - t_{n-2}) + \omega_0(t_n - t_{n-1}))(t_{n-1/2} - t_{n-1}) - \frac{1}{2}(\gamma_2\omega_{-1} - \omega_1\gamma_0)(t_n - t_{n-2})^2 \\
&- \frac{1}{2}(\gamma_2\omega_0 - \gamma_1\omega_1)(t_n - t_{n-1})^2 \\
&+ \frac{1}{2}(\omega_{-1}(t_n - t_{n-2})^2 + \omega_0(t_n - t_{n-1})^2)(t_{n-1/2} - t_{n-1}) + \frac{1}{6}(\gamma_2\omega_{-1} - \omega_1\gamma_0)(t_n - t_{n-2})^3 \\
&+ \frac{1}{6}(\gamma_2\omega_0 - \gamma_1\omega_1)(t_n - t_{n-1})^3 \\
&= (t_n - t_{n-1/2})(t_{n-1/2} - t_{n-1}) - \gamma_2(t_n - t_{n-1/2}).
\end{aligned}
$$

We identify the terms of the same power to obtain a linear system in $\{\omega_i\}_i$. To make the system easier to read, we introduce the quantities:

$$\frac{(t_{n-1/2} - t_{n-1})}{(t_n - t_{n-1})} = a_1, \qquad \frac{(t_n - t_{n-1/2})}{(t_n - t_{n-1})} = 1 - a_1, \qquad \frac{(t_n - t_{n-2})}{(t_n - t_{n-1})} = \varepsilon_n,$$

yielding the following linear system:

$$\begin{cases} \omega_{-1} + \omega_0 + \omega_1 + \omega_2 = 0 \\ (a_1 + \gamma_2\varepsilon_n)\omega_{-1} + (a_1 + \gamma_2)\omega_0 - (\varepsilon_n\gamma_0 + \gamma_1)\omega_1 + (a_1)\omega_2 = -(1 - a_1)\gamma_2 \\ (2\varepsilon_n a_1 + \gamma_2\varepsilon_n^2)\omega_{-1} + (2 a_1 + \gamma_2)\omega_0 - (\varepsilon_n^2\gamma_0 + \gamma_1)\omega_1 = -2(1 - a_1)a_1 \\ (3\varepsilon_n^2 a_1 + \gamma_2\varepsilon_n^3)\omega_{-1} + (3 a_1 + \gamma_2)\omega_0 - (\varepsilon_n^3\gamma_0 + \gamma_1)\omega_1 = 0. \end{cases}$$

For each value of a_1 and ε_n, this system must be solved to obtain the coefficients $\{\omega_i\}_i$. By manipulating the terms, we prove that:

$$\varepsilon_n = (1 - a_1) + a_1\varepsilon_n', \quad \text{with} \ \varepsilon_n' = 1 + \frac{r_n}{a_1} \ \text{and} \ r_n = \frac{t_{n-1} - t_{n-2}}{t_n - t_{n-1}}. \tag{19}$$

Thus, the solution of the above system is given by:

$$\begin{aligned} \omega_{-1} &= -\frac{(a_1 - 1)\left(3a_1^3 + (3r_n - 4)a_1^2 + (r_n^2 - 2r_n + 2)a_1 + r_n\right)}{(3a_1^2 + 2(r_n - 1)a_1 - r_n)(1 + r_n)r_n(a_1 + r_n)} \\[2mm] \omega_0 &= \frac{(1 + r_n)(a_1 - 1)\left(3a_1^3 + (2r_n - 4)a_1^2 - 2(r_n - 1)a_1 + r_n\right)}{(3a_1^2 + 2(r_n - 1)a_1 - r_n)r_n a_1} \\[2mm] \omega_1 &= -\frac{(1 + r_n)(a_1 - 1)(2a_1 + r_n)}{(3a_1^2 + 2(r_n - 1)a_1 - r_n)(a_1 + r_n)a_1} \\[2mm] \omega_2 &= -\frac{(a_1 - 1)^2\left((3r_n + 6)a_1 + 2r_n^2 + 3r_n\right)}{(3a_1^2 + 2(r_n - 1)a_1 - r_n)(1 + r_n)}. \end{aligned} \tag{20}$$

Returning to the algebraic Equation (18), a fourth-order numerical approximation of y_n can be obtained without using y_{n-2} but provided $\omega_{-1} = 0$. That is,

$$3a_1^3 + (3r_n - 4)a_1^2 + (r_n^2 - 2r_n + 2)a_1 + r_n = 0. \tag{21}$$

Solving this equation in terms of a_1 will help formulate the two-step composition of the BDF. Note that the trivial case $a_1 = 1$ causes all the coefficients $\omega_i = 0, i = -1, 0, 1, 2$ to vanish, thus preventing the composition from being achieved. Thereafter, we will present the composition algorithm of BDF with a fixed time step.

3.4. Algorithm of Composed BDF-2 Scheme with Fixed Time Step

Herein, the time steps t_n are equidistant, which gives $r_n = 1$ and $\varepsilon_n = 2$ for all $n > 2$. Therefore, $a_1 \neq 1$ is the solution for $\omega_{-1} = 0$, yielding:

$$(a_1 - 1)(3a_1^3 - a_1^2 + a_1 + 1) = 0.$$

That results in a complex step size:

$$a_1 = \frac{1}{9}\left(-\frac{8}{b}\left(\frac{1}{2} - \mathbf{i}\frac{\sqrt{3}}{2}\right) - b\left(\frac{1}{2} + \mathbf{i}\frac{\sqrt{3}}{2}\right) + 1\right), \quad \text{with} \ b = \left(\frac{2\sqrt{19}}{\sqrt{3}} - 134\right)^{1/3}.$$

Hence, ε'_n, a_2, and the coefficients γ_i from (15) are computed as follows:

$$\varepsilon'_n = 1 + \frac{1}{a_1}, \qquad a_2 = 1 - a_1, \qquad \gamma_0 = \frac{a_1^2}{a_1 + 1}, \qquad \gamma_1 = \frac{a_1 + 1}{a_1}, \qquad \gamma_2 = \frac{a_1 + 2}{a_1 + 1}.$$

From (20), we also compute the coefficients $\{\omega_i\}_i$:

$$\omega_{-1} = 0, \qquad\qquad \omega_0 = \frac{2(a_1 - 1)(3a_1^3 - 2a_1^2 + 1)}{(3a_1^2 - 1)a_1},$$

$$\omega_1 = -\frac{2(a_1 - 1)(2a_1 + 1)}{(3a_1^2 - 1)(a_1 + 1)a_1}, \qquad\qquad \omega_2 = -\frac{(a_1 - 1)^2(9a_1 + 5)}{2(3a_1^2 - 1)}.$$

Algorithm 1 can be summarized as follows:

Algorithm 1 Composed BDF-2 with fixed time step.

1: Set fixed-point tolerance `tol` and time step Δt
2: Set initial conditions ($n = 0$): y_0 and $y_{-1} = y_0$
3: Compute a_1, γ_i and ω_i, with $i = 1, 2, 3$
4: **for** $n = 1, \dots, n_{\max}$ **do**
5:     Update time $t_{n-1/2} = t_{n-1} + a_1 \Delta t$
6:     Initialize $y^0_{n-1/2}$
7:     **for** $k = 0, \dots, k_{\max}$ **do**
8:         Compute $\gamma_2 y^{k+1}_{n-1/2} + a_1 \Delta t\, f(t_{n-1/2}, y^{k+1}_{n-1/2}, y^k_{n-1/2}) = -\gamma_1 y_{n-1} - \gamma_0 y_{n-2}$
9:         **if** $|y^{k+1}_{n-1/2} - y^k_{n-1/2}| < $ `tol` **then**
10:             Update solution $y_{n-1/2} = y^{k+1}_{n-1/2}$
11:             break
12:         **end if**
13:     **end for**
14:     Update time $t_n = t_{n-1/2} + a_2 \Delta t$ with $a_2 = 1 - a_1$
15:     Initialize $\widehat{y_n}^0$
16:     **for** $k = 0, \dots, k_{\max}$ **do**
17:         Compute $\omega_2 \widehat{y_n}^{k+1} + a_2 \Delta t_k\, f(t_n, \widehat{y_n}^{k+1}, \widehat{y_n}^k) = -\omega_1 y_{n-1/2} - \omega_0 y_{n-1}$
18:         **if** $|\widehat{y_n}^{k+1} - \widehat{y_n}^k| < $ `tol` **then**
19:             Update solution $\widehat{y_n} = \widehat{y_n}^{k+1}$
20:             break
21:         **end if**
22:     **end for**
23:     Set $y_n = \mathrm{Re}(\widehat{y_n})$ as approximation of $y(t_n)$
24:     **if** $t_{n+1} \geqslant T$ **then**
25:         break
26:     **end if**
27: **end for**

3.5. Algorithm for Composing BDF-2 with Adaptive Time Step

The algorithm is adapted to solve the stiff problem based on the composed BDF-2 method with adapted time steps. Its structure is similar to that presented in Algorithm 1. Nevertheless, caution is essential for calculating the parameters a_1, γ_i, and ω_i, with $i = 1, 2, 3$, which must now be updated at each time step.

The time step is adapted according to the imaginary part, which can represent a control criterion for the temporal integration error, as will be shown in the numerical examples. The temporal adaptation is performed in such a way that the temporal integration error does not exceed a predefined accuracy requirement TOL. For $n \geqslant 0$ and given the order p of the integrator, the adapted time step Δt_{n+1} is calculated as follows:

$$\Delta t_{n+1} = \Delta t_n \times \sqrt[p+1]{\frac{\mathrm{TOL}}{C\,\mathrm{Im}(\widehat{y_n})}} \tag{22}$$

The algorithm is provided in Algorithm 2.

Algorithm 2 Composed BDF-2 with adaptive time steps.

1: Set fixed-point tolerance `tol`, time $t = 0$, and initial time step Δt_1
2: Set initial conditions: y_0 and $y_{-1} = y_0$
3: **for** $n = 1, \ldots, n_{\max}$ **do**
4:      Compute r_n from (19) and a_1 from (21)
5:      Compute γ_i, with $i = 1, 2, 3$ from (15)
6:      Update time $t_{n-1/2} = t_{n-1} + a_1 \Delta t_n$
7:      Initialize $y_{n-1/2}^0$
8:      **for** $k = 0, \ldots, k_{\max}$ **do**
9:         Compute $\gamma_2 y_{n-1/2}^{k+1} + a_1 \Delta t_n f(t_{n-1/2}, y_{n-1/2}^{k+1}, y_{n-1/2}^k) = -\gamma_1 y_{n-1} - \gamma_0 y_{n-2}$
10:        **if** $|y_{n-1/2}^{k+1} - y_{n-1/2}^k| < $ `tol` **then**
11:           Update solution $y_{n-1/2} = y_{n-1/2}^{k+1}$
12:           break
13:        **end if**
14:      **end for**
15:      Update time $t_n = t_{n-1/2} + a_2 \Delta t_n$ with $a_2 = 1 - a_1$
16:      Compute ω_i, with $i = 1, 2, 3$ from (20)
17:      Initialize $\widehat{y_n}^0$
18:      **for** $k = 0, \ldots, k_{\max}$ **do**
19:         Compute $\omega_2 \widehat{y_n}^{k+1} + a_2 \Delta t_n f(t_n, \widehat{y_n}^{k+1}, \widehat{y_n}^k) = -\omega_1 y_{n-1/2} - \omega_0 y_{n-1}$
20:        **if** $|\widehat{y_n}^{k+1} - \widehat{y_n}^k| < $ `tol` **then**
21:           Update solution $\widehat{y_n} = \widehat{y_n}^{k+1}$
22:           break
23:        **end if**
24:      **end for**
25:      Set $y_n = \mathrm{Re}(\widehat{y_n})$ as approximation of $y(t_n)$
26:      **if** $t_{n+1} \geqslant T$ **then**
27:        break
28:      **end if**
29:      Adapt the time step Δt_{n+1} from (22)
30: **end for**

---

4. Numerical Approximation of the Fluid/Membrane Problem

In this section, we present the main aspects of the numerical discretization. For ease of presentation, we provide the temporal discretization of both fluid and level-set problems before applying the composition technique. A penalty method is introduced to handle the surface divergence constraint, which reduces the system size and allows the use of classical Navier–Stokes solvers. The level-set problem is solved using the streamline upwind Petrov–Galerkin (SUPG) stabilization, while a fixed-point algorithm allows a tightly coupled iterative approach for the fluid/vesicle problem.

4.1. Time Discretization of the Fluid Problem

Let us divide the time interval $[0, T]$ into subintervals $[t_n, t_{n+1})$, with $n = 0, \ldots$ of variable time steps Δt_n. For any $n \geqslant 0$, the unknowns $\boldsymbol{u}_n$, p_n, and φ_n at time step n are iteratively computed. Semi-discrete geometric quantities and surface operators (e.g., **n**, H, $\boldsymbol{I} - \mathbf{n} \otimes \mathbf{n}, \ldots$) at time t_n are endowed with a subscript n. The semi-discretized membrane bending force at t_n is written as: $\boldsymbol{F}_n = 1/\mathrm{Ca} \left\{ \Delta_{s,n} H_n + H_n^3/2 \right\} \mathbf{n}_n$.

Hereafter, we present the fluid problem semi-discretized in time. Without loss of generality, we assume equal densities of external and encapsulated fluids $\rho_i = \rho_o$, since no dependence of densities on cellular behaviors has been observed in the literature [83]. Steps 1 and 2 of the composition algorithm both involve a second-order backward difference formula with varying time steps. Let δt_n and $\delta_i, i = 0, 1, 2$ represent the time step and BDF-2 coefficients, respectively; they correspond to $a_1 \Delta t_n$ and γ_i in Step 1 and to $a_2 \Delta t_n$ and ω_i in

Step 2. In the following, we simply present the semi-discretized problem corresponding to $(y_n, y_{n-1}) = Y^{BDF2}_{\delta t_n, \delta_i}(y_{n-1}, y_{n-2})$.

The time derivative term of u in the momentum equation is first discretized using a second-order backward difference formula:

$$\frac{\partial u}{\partial t}(t, x) = \frac{\gamma_2 u(t, x) + \gamma_1 u(t - \delta t_n, x) + \gamma_0 u(t - 2\delta t_n, x)}{\delta t_n} + \mathcal{O}\left(\delta t_n^2\right).$$

To subsequently present the penalty approach, we also use the method of characteristics; see, e.g., [84]. For any $n > 0$, let $\mathbf{u}^* = 2\mathbf{u}_{n-1} - \mathbf{u}_{n-2}$ be a second-order extrapolation of $\mathbf{u}$ at time t_n, with $\mathbf{u}_{-1} = \mathbf{u}_0$ and $\mathbf{u}_{-1}$ being a convenient notation. We denote by $X_{2,n-1}$ and $X_{2,n}$ the second-order characteristics terms using the predicted $\mathbf{u}^*$. We consider a second-order approximation of the Lagrange derivative. Given an approximation of φ_n and Γ_n, the time-discretized problem (8) reads:

Find $\mathbf{u}_n$, p_n, and λ_n such that:

$$\frac{Re}{\delta t_n}(\gamma_2 \mathbf{u}_n + \gamma_1 \mathbf{u}_{n-1}oX_{2,n-1} + \gamma_0 \mathbf{u}_{n-2}oX_{2,n-2})$$

$$-\mathbf{div}(2\eta_\varepsilon^*(\mathbf{D}(u_{n-1}), \varphi_n)\,\mathbf{D}(\mathbf{u}_n)) + \nabla p_n \;=\; \mathbf{0} \quad \text{in } \Lambda \backslash \partial\Omega_n, \tag{23a}$$

$$\mathrm{div}\,\mathbf{u}_n \;=\; 0 \quad \text{in } \Lambda, \tag{23b}$$

$$\mathrm{div}_{s,n}\,\mathbf{u}_n \;=\; 0 \quad \text{on } \Gamma_n, \tag{23c}$$

$$[\![\mathbf{u}_n]\!] \;=\; \mathbf{0} \quad \text{on } \Gamma_n, \tag{23d}$$

$$[\![2\eta_\varepsilon^*(\mathbf{D}(u_{n-1}), \varphi_n)\,\mathbf{D}(\mathbf{u}_n) - p_n\mathbf{I}]\!].\mathbf{n}_n - F_n + H_n\lambda_n\mathbf{n}_n - \nabla_{s,n}\lambda_n \;=\; \mathbf{0} \quad \text{on } \Gamma_n, \tag{23e}$$

$$\mathbf{u}_n \;=\; \mathbf{u}_b \quad \text{on } \Sigma_D. \tag{23f}$$

To reduce the size of the system and allow the use of standard Navier–Stokes solvers by relaxing the constraint (23c), we present in the following subsection a penalized form of this last problem.

4.2. Penalty Method

We point out that the velocity belongs to the admissible space $\mathbb{K}(V) \cap \mathbb{L}$, with:

$$\mathbb{K}(V) = \left\{\mathbf{v} \in \mathbb{V}(V) \text{ s.t. } \mathrm{div}\,\mathbf{v} = 0 \text{ in } \Lambda\right\} \text{ and } \mathbb{L} = \left\{\mathbf{v} \in \left(H^1(\Lambda)\right)^2 \text{ s.t. } \mathrm{div}_s\,\mathbf{v} = 0 \text{ on } \Gamma\right\}.$$

To remove the inextensibility (23c), we write the problem as a minimization problem:

$$\mathbf{u}_n = \underset{\mathbf{v} \in \mathbb{K}(t, V_b) \cap \mathbb{L}}{\arg\inf} J_n(\mathbf{v}), \tag{24}$$

with

$$J_n(\mathbf{v}) = \frac{Re\,\gamma_2}{2}\int_\Lambda \mathbf{v}^2 + \int_\Lambda \eta_\varepsilon^*(\mathbf{D}(u_{n-1}), \varphi_n)|2\,\mathbf{D}(\mathbf{v})|^2$$

$$- \int_\Lambda (\gamma_1\mathbf{u}_{n-1}oX_{2,n-1} + \gamma_0\mathbf{u}_{n-2}oX_{2,n-2})\mathbf{v} - \int_{\Gamma_n} F_n.\mathbf{v}.$$

We approach the minimization problem (24) with another minimization problem by penalizing the surface divergence-free condition. The membrane tension field λ_n no longer appears as unknown in the problem to be solved. Let ε_λ be a small penalty parameter. The velocity field is approximated by another satisfying the penalized problem. The same notation is used for the approximate velocity, which is given by:

$$\mathbf{u}_n = \underset{\mathbf{v} \in \mathbb{K}(t, V_b)}{\arg\inf} J_{n,\varepsilon_\lambda}(\mathbf{v}),$$

with

$$J_{n,\varepsilon_\lambda}(\mathbf{v}) = J_n(\mathbf{v}) + \frac{1}{2\varepsilon_\lambda}\int_{\Gamma_n}(\mathrm{div}_{\mathrm{s,n}}\,\mathbf{v})^2.$$

The mixed velocity/pressure formulation results from a saddle point formulation:

$$(\mathbf{u}_n; p_n) = \underset{\mathbf{v}\,\in\,\mathbb{V}(V_b)}{\arg\inf}\;\underset{q\in L^2(\Lambda)}{\sup}\left\{J_{n,\varepsilon_\lambda}(v) + \int_\Lambda q\,\mathrm{div}\,v\right\}.$$

The variational formulation is obtained based on the corresponding optimality conditions. After approximation of surface integrals over Γ as integrals over the entire domain Λ, the weak formulation is given by:
find $u_n \in \mathbb{V}(V_b)$ and $p_n \in L_0^2(\Lambda)$ such that:

$$\frac{Re\,\gamma_2}{\delta t_n}\int_\Lambda u_n\cdot v + \int_\Lambda 2\eta_\varepsilon^*(\mathbf{D}(u_{n-1}),\varphi_n)\,\mathbf{D}(u_n):\mathbf{D}(\mathbf{v}) - \int_\Lambda p_n\,div\,v$$

$$+\frac{1}{\varepsilon_\lambda}\int_\Lambda |\boldsymbol{\nabla}\varphi_n|\delta_\varepsilon(\varphi_n)\,div_{s,n}(u_n)\,div_s(v)$$

$$= \int_\Lambda\left(|\boldsymbol{\nabla}\varphi_n|\delta_\varepsilon(\varphi_n)\,F_n - \gamma_1 u_{n-1}oX_{2,n-1} - \gamma_0 u_{n-2}oX_{2,n-2}\right)\cdot v, \quad \forall v\in\mathbb{V}(0),$$

$$\int_\Lambda q\,div\,u_n = 0, \qquad\qquad\qquad\qquad\qquad\qquad \forall q\in L_0^2(\Lambda). \quad (25)$$

We proceed with finite elements for the spatial discretization. Let us consider a partition $\mathscr{T}_h$ of Λ consisting of geometrically conformal triangular elements K, such that $\overline{\Lambda} = \underset{K\in\mathscr{T}}{\cup}$. For any $K\in\mathscr{T}$, the mesh size h is the diameter of the largest mesh element $h = \max h_K$. Let P_h^k be the h-dependent discrete finite element space spanned by the Lagrange polynomials of degree $k\geqslant 1$. We consider the inf-sup stable finite element (Taylor–Hood) $[\mathsf{P}_h^{k+1}]^2 - \mathsf{P}_h^k$ for the discretization of u and p. The resulting nonlinear problem (25) corresponds to a classical symmetric and non-singular sparse matrix. The system is solved interatively with a preconditioned GMRES algorithm. Fixed-point iterations are also considered at each time step n to allow better numerical stability.

4.3. Level Set Problem

In a similar way, the level-set equation is discretized in time using a BDF-2 scheme. We also proceed with stabilization using the streamline upwind Petrov–Galerkin (SUPG) [85] method. In fact, we consider a classical stabilization term, denoted by $S(\tau_K;\varphi,\psi)$, in (8a) that consists of adding some diffusion in the streamline direction. The parameter τ_K is the streamline diffusion coefficient that is proportional to the mesh size h_K in the mesh element K and depends on the discretized velocity $u_{n,h}$. We choose:

$$\tau_K = \frac{h_K}{s_c\|u_{n,h}\|_{\infty,K}}, \quad K\in\mathscr{T}_h,$$

with s_c a scaling factor [86]. Given u_n, the time-discretized level-set equation is given by:
find $\varphi_n\in\mathbb{X} = W^{1,\infty}(\Lambda)\cap H^1(\Lambda)$ such that:

$$\int_\Lambda\frac{\gamma_2\varphi_n + \gamma_1\varphi_{n-1} + \gamma_0\varphi_{n-2}}{\delta t_n}\psi + \int_\Lambda(u_n\cdot\boldsymbol{\nabla}\varphi_n)\psi + \int_\Lambda S(\tau_K;\varphi_n,\psi) = 0, \qquad (26)$$

for all test functions $\psi\in\mathbb{X}$. Moreover, we regularly solve for a few iterations the so-called redistancing problem, which helps to keep the level-set solution close to a signed distance function [31].

Appendix A provides additional insights into the implementation of the composition technique applied to the level set problem.

5. Numerical Results

In this section, we conduct a set of numerical experiments in the case of ordinary and partial differential equations to assess the main features of the proposed method. In Example 1, an ODE test case is presented to study both the convergence properties of the composed BDF-2 scheme and the time-stepping strategy based on the imaginary part criterion. Example 2 is dedicated to the validation of the numerical framework in terms of biophysical significance. Several validation tests are presented with comparisons to known numerical and experimental results in the published literature. Finally, in Example 3, we study the effect of non-Newtonian behavior on the membrane dynamics and present some preliminary results.

Numerical simulations have been implemented using the finite element library FEniCS [87].

5.1. Example 1: One-Dimensional Test Case—Accuracy-Order Analysis

In this example, we numerically solve the following stiff IVP using adapted time steps:

$$\frac{dy}{dt} = y^2 - y^3, \quad t \in \left[0, \frac{2}{\varkappa}\right]$$
$$y(0) = \varkappa < 1.$$

Note that the independent variable belongs to an interval that depends on the initial value. The IVP has a known exact solution $y(t) = \dfrac{1}{W(ae^{a-t}) + 1}$, where $a = \frac{1}{\varkappa} - 1$ and $W(z)$ is the Lambert function defined as the solution for the equation $We^W = z$. The solution starts to slowly increase from $y(0) = \varkappa$ before showing a stiff variation around $t = 1/\varkappa$; it eventually reaches a stationary state $y \to 1$ when $t \to \infty$. The closer the $\varkappa$ is to zero, the steeper the curve around $t = 1/\varkappa$. Figure 3 shows the exact solution for different values of the parameter $\varkappa$.

For a precise resolution, the numerical scheme must allow the use of a variable time step so that the latter is reduced when strong variations of the solution are observed, while it is increased otherwise. The time-stepping strategy could be based on an error estimate of the numerical approximation so that the time step is adapted up to a given tolerance. If the error is less than a tolerance, the step time is increased, and vice versa if not. We first compute the solution for a fixed time step equal to $\Delta t = 2/640\varkappa$ to see how the imaginary part of the composed discrete flow behaves and whether this could represent an appropriate error estimate. Figure 4 plots the evolution of the error between the approximate solution, given by the real part of the composed discrete flow, and the exact solution. It also displays the imaginary part of the composed scheme. The results clearly show that both curves have the same pattern: they increase before reaching a maximum value around $t = 1/\varkappa$, and they decrease afterwards.

Consequently, the imaginary part represents a good error estimate and a precise criterion for adapting the time step size. For different parameters $\varkappa$, Figure 5 describes the adapted time steps throughout the simulation periods. The results show that the time step is correctly reduced to follow the dynamics of the solution when large variations occur in the region of stiff variations of y_n with $n > 0$. For $\varkappa = 0.01$, we plot in the same graph the adapted time steps as well as the approximate solution and the error evolution. More importantly, Figure 6 shows the success of the method to control the error and consequently achieve the desired accuracy by adapting the time step size; the error remains less than 10^{-11}.
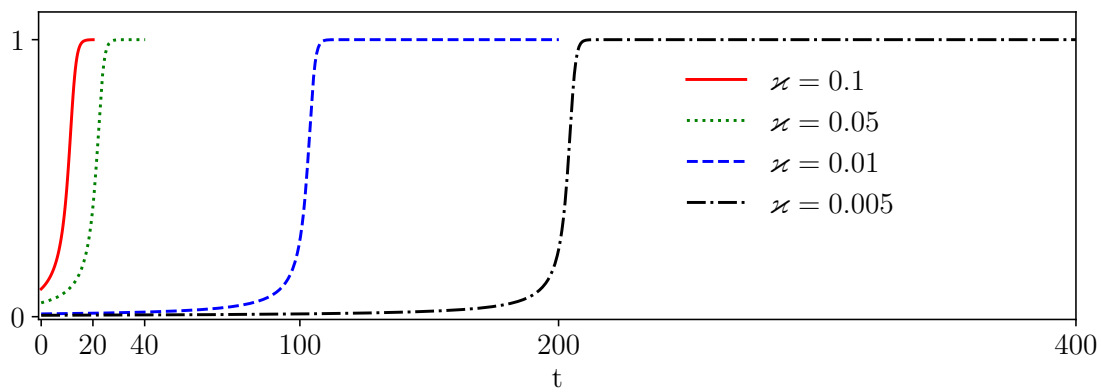
Figure 3. Graph of the exact solution of the initial value problem for different choices of the parameter $\varkappa = 0.1, 0.05, 0.01, 0.005$.
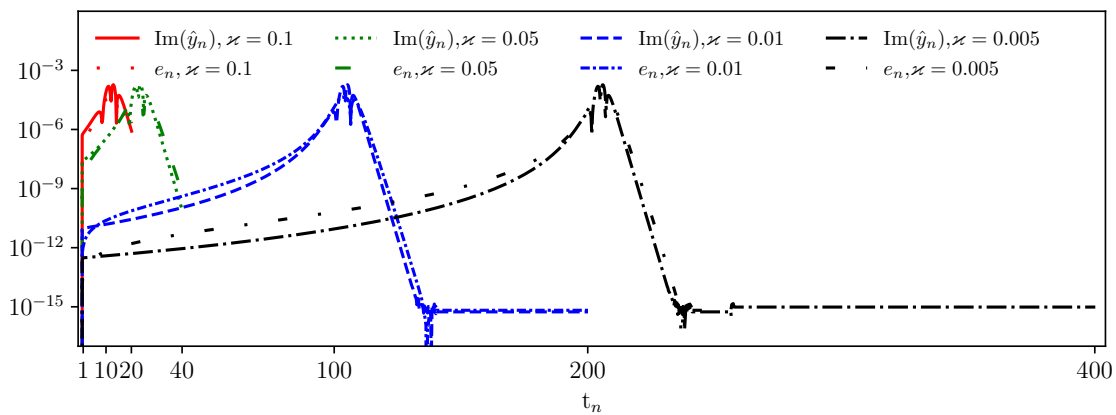
Figure 4. Time evolution of (i) the error between the exact and computed approximate solutions $e_n = |y_n - y(t_n)|$ and (ii) the error indicator based on the imaginary part $\mathrm{Im}(haty_n)$. Different values of $\varkappa = 0.1, 0.05, 0.01, 0.005$ are considered.
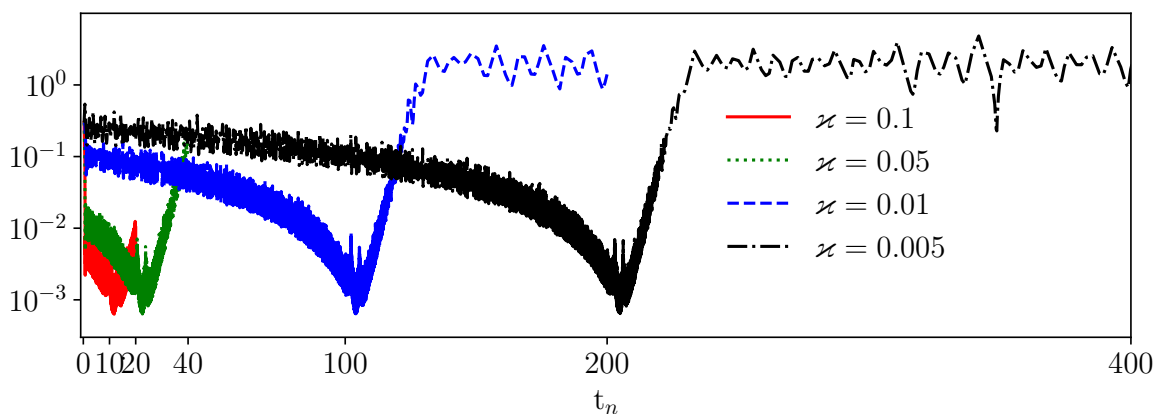

Figure 5. Evolution of the adapted time step size Δt_n with respect to time t using the imaginary part of the composed numerical flow as an adaptation criterion. The IVP is solved for different parameters $\varkappa = 0.1, 0.05, 0.01, 0.005$.
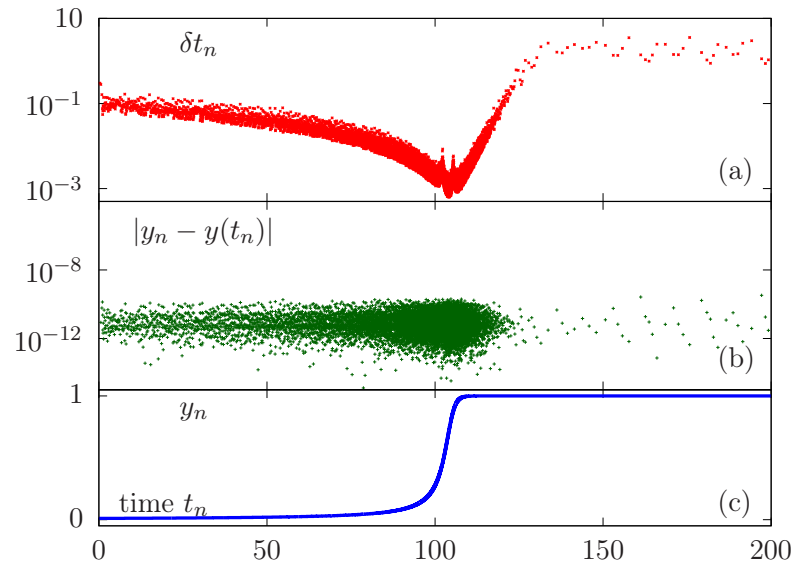
Figure 6. Quantitative study of accuracy obtained using adapted time steps. Plot of evolution in time of the time step size (**a**), error (**b**), and approximated solution (**c**) for $\varkappa = 0.01$.

The time accuracy of the numerical approximations is studied by calculating the absolute errors for successively refined time steps compared to the exact solution. We consider the standard BDF-2 scheme and its double composition. The change in error is displayed in Figure 7, showing that optimal convergence is achieved. Convergence rates for basic and composed schemes are reported in Table 1.
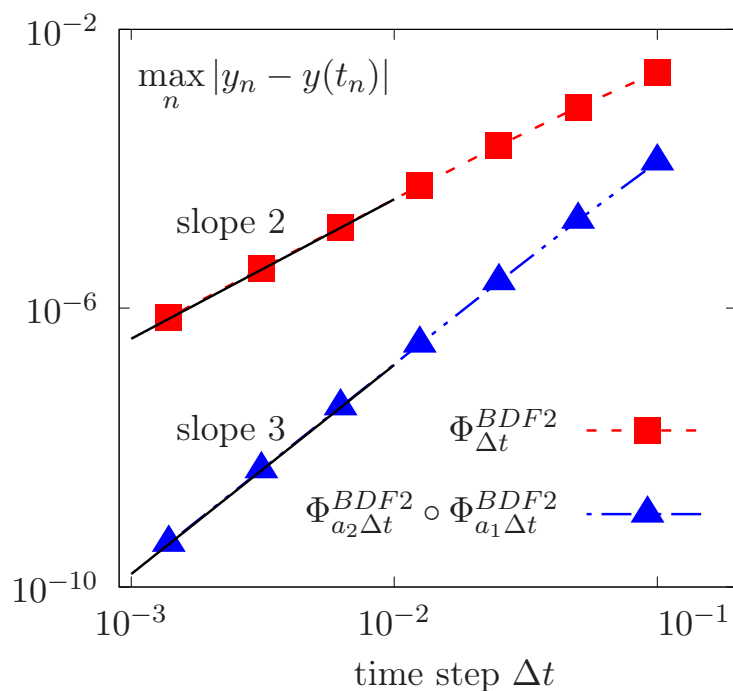
Figure 7. Temporal convergence results of the error between the exact solution and the calculated solution for different time integration methods using $Y_{\Delta t}^{\text{BDF2}}$ and the double flow composition $Y_{a_2\Delta t}^{\text{BDF2}} \circ Y_{a_1\Delta t}^{\text{BDF2}}$. Uniform time steps are considered.

In the following, the time-stepping strategy will be used on a more complex PDE problem simulating the dynamics of blood cells in flow.

Table 1. Table showing the error convergence rates between the exact and approximate solution in Figure 7, showing second-order and third-order for BDF-2 and its dual composition, respectively.

$1/\Delta t$	20	40	80	160	320	720
$\Upsilon_{\Delta t}^{\mathrm{BDF2}}$	1.65	1.83	1.92	1.96	1.98	1.99
$\Upsilon_{a_2 \Delta t}^{\mathrm{BDF2}} \circ \Upsilon_{a_1 \Delta t}^{\mathrm{BDF2}}$	2.777	2.925	2.975	2.991	2.996	2.998

5.2. Example 2: Membrane Dynamics in a Newtonian Fluid under Simple Shear Flow

In this example, we perform numerical simulations of the dynamics of a two-dimensional vesicle under Newtonian shear flow. The Bingham parameter is then set to zero. A sketch of the problem setup is provided in Figure 1. We study the dynamics of a vesicle of reduced surface $\Xi_{2D} = 0.847$ immersed in an initially stationary fluid. The membrane is confined in a square domain with confinement parameter $\alpha = 1/2$. It initially has an ellipse shape, with semi-major and semi-minor axes of $\alpha/2$ and $\alpha/4$, respectively, and is located at the center of the domain; see Figure 8 (left). The physical parameters of the simulation are: Re $= 5.6 \times 10^{-3}$ and Ca $= 8 \times 10^4$. Here, we consider a uniform time step $\Delta t = 5 \times 10^{-3}$. Quasi-uniform unstructured meshes are generated using the *mshr* generator available in the FEniCS packages. Unless otherwise specified, we define $\varepsilon_\lambda \approx h^{1.5}$ in our simulations, where h is the mesh size. We then provide a numerical study of the optimal choice of the penalty parameter ε_λ.

Under simple shear flow conditions, an inextensible two-dimensional vesicle undergoes two characteristic major dynamic behaviors known as tank-treading and tumbling regimes. For fixed physical parameters, while varying the viscosity contract between the internal fluid and the external fluid, the dynamics of the membrane change drastically. Indeed, for small viscosity ratios, the vesicle begins to rotate and reaches a stable shape with a fixed inclination angle with respect to the flow direction. The membrane continues to tank-tread around the internal fluid, which represents the tank-treading movement. By increasing the viscosity ratio above a threshold value of β, the tank-treading motion is supressed. The vesicle then behaves like a rigid elastic body that undergoes a periodic rotational movement in flow like a rigid body around its center of mass; this is the tumbling regime.

5.2.1. Tank-Treading Regime

We first set the viscosity ratio $\beta = 1$. Figure 8 provides snapshots showing the dynamic behaviors of the vesicle until reaching the stationary tank-treading regime. We also plot in Figure 9 the temporal evolution of the membrane inclination angle, showing the convergence towards an equilibrium steady state. In Figure 10, we provide the variation of the relative area and relative perimeter errors throughout the simulation period, showing good conservation of area and perimeter as required by the cell model.

Figure 11 shows the temporal evolution of the imaginary part, which is important to perform the adaptation of the time step afterwards. It can be seen that the imaginary part follows the dynamics of the membrane, where larger values are obtained as the membrane is away from the stationary tank-treading shape and begin to decrease until the equilibrium regime is reached.
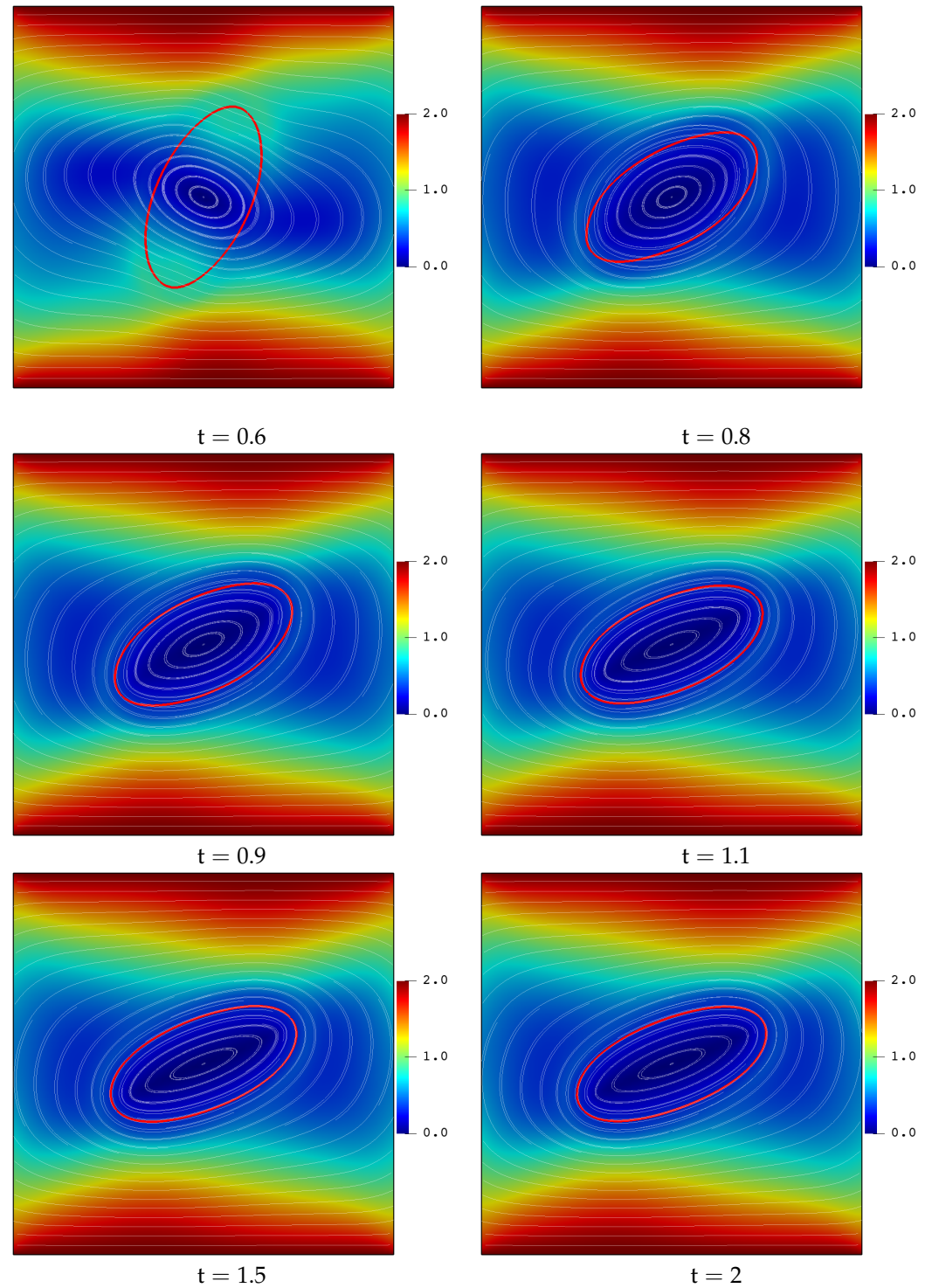
Figure 8. Snapshots showing the deformations and movement of a membrane following a tank-treading regime in simple shear flow. Snapshots showing membrane deformation (red color), velocity amplitude, and streamlines. Physical parameters: $\Xi_{2D} = 0.847$, $\beta = 1$, $\mathrm{Re} = 5.6 \times 10^{-3}$, $\mathrm{Ca} = 8 \times 10^4$, and $\mathrm{Bn} = 0$.
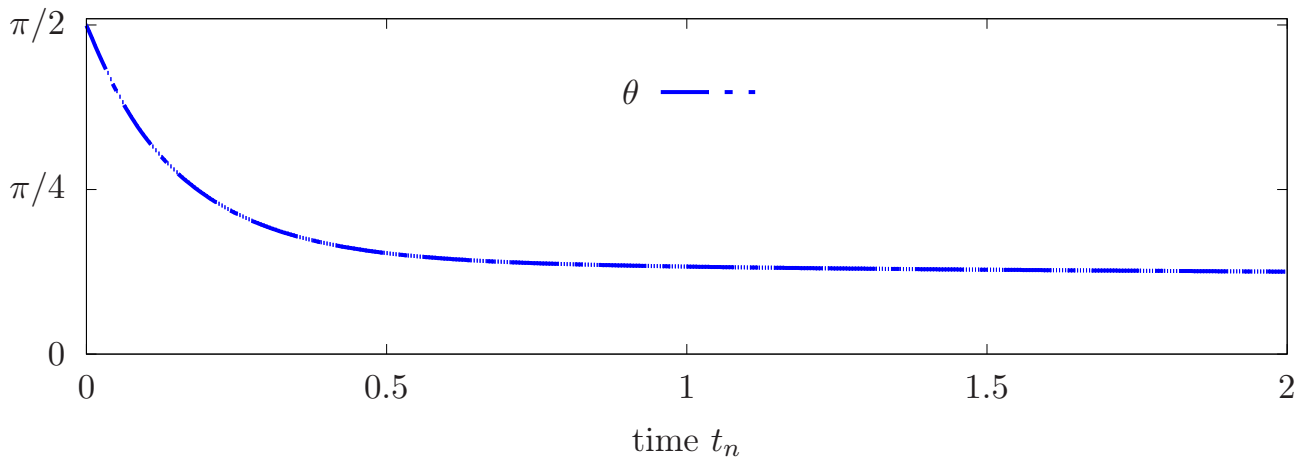
Figure 9. Time evolution of the membrane's inclination angle for a vesicle in a tank-treading movement under simple shear flow. Physical parameters: $\Xi_{2D} = 0.847$, $\beta = 1$, $\mathrm{Re} = 5.6 \times 10^{-3}$, $\mathrm{Ca} = 8 \times 10^{4}$, and $\mathrm{Bn} = 0$.
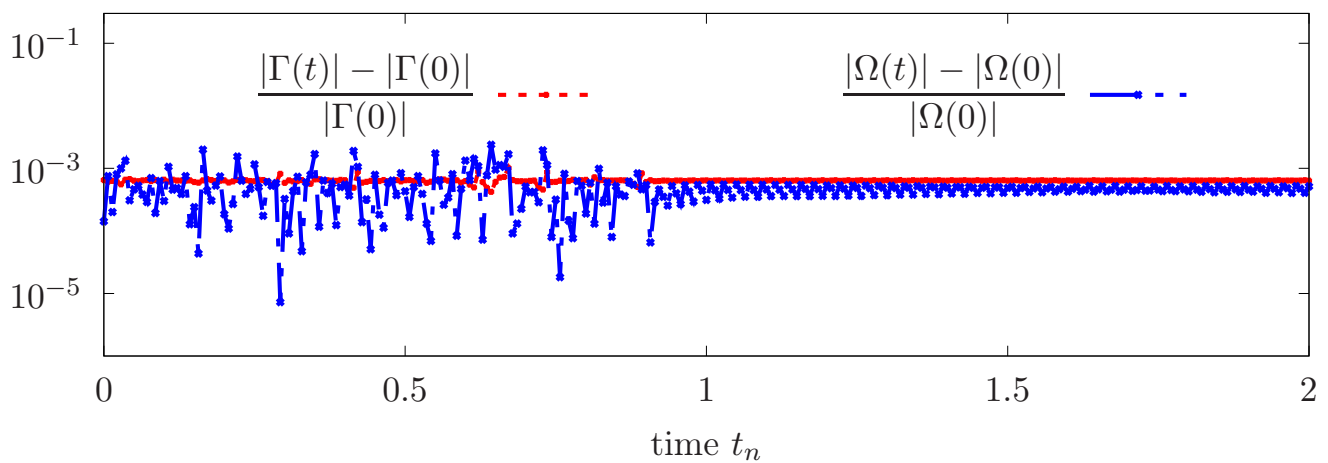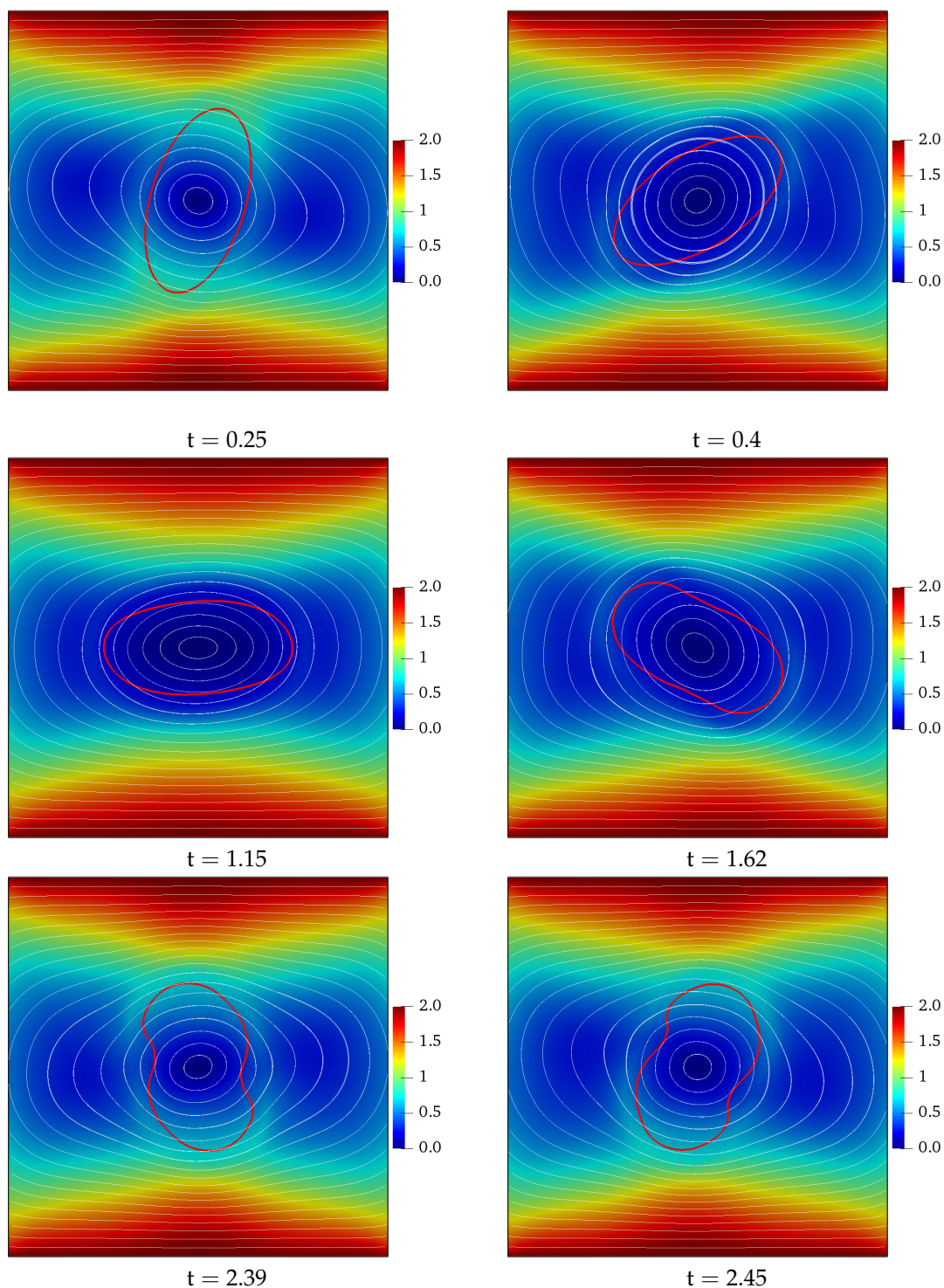

Figure 10. Time evolution of the relative error in the membrane's area and perimeter for a vesicle in a tank-treading movement. Logarithmic scale is used on the y axis. Physical parameters: $\Xi_{2D} = 0.847$, $\beta = 1$, $\mathrm{Re} = 5.6 \times 10^{-3}$, $\mathrm{Ca} = 8 \times 10^{4}$, and $\mathrm{Bn} = 0$.
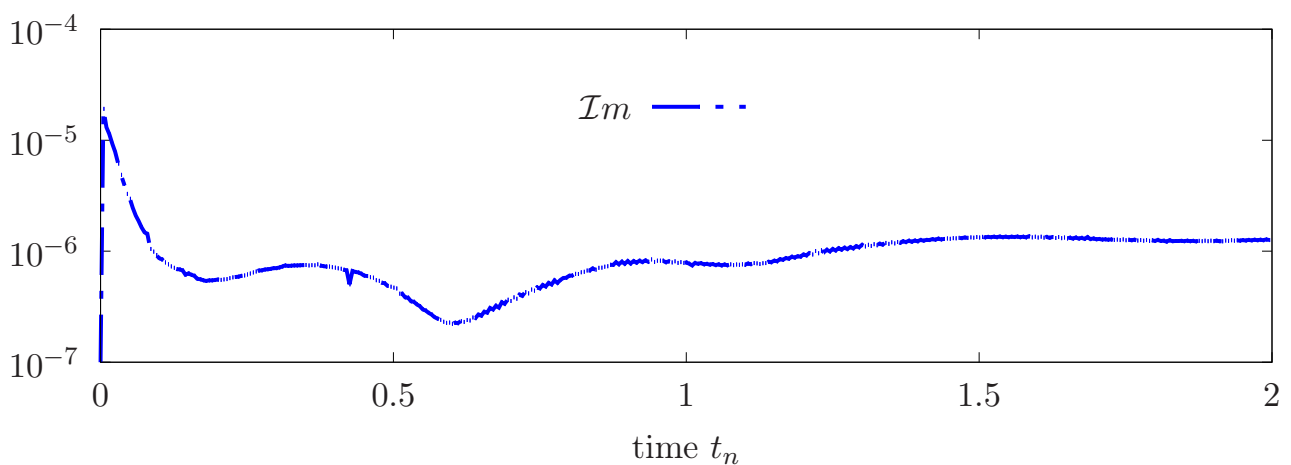
Figure 11. Error estimation based on the imaginary part throughout the simulation period for a vesicle in a tank-treading movement. Logarithmic scale is used on the y axis. Physical parameters: $\Xi_{2D} = 0.847$, $\beta = 1$, $\mathrm{Re} = 5.6 \times 10^{-3}$, $\mathrm{Ca} = 8 \times 10^{4}$, and $\mathrm{Bn} = 0$.

5.2.2. Tumbling Regime

We now set a viscosity ratio $\beta = 10$, resulting in a regime change towards a tumbling movement. The simulation is run for one period of complete rotation of the vesicle. Snapshots of the membrane at successive instants are provided in Figure 12.

We also provide in Figure 13 the temporal evolution of the area and perimeter, showing good conservation properties.

$t = 0.25$ $t = 0.4$

$t = 1.15$ $t = 1.62$

$t = 2.39$ $t = 2.45$

Figure 12. Tumbling motion of a vesicle immersed in a Newtonian fluid under simple shear flow. Snapshots showing membrane deformation (red color), velocity amplitude, and streamlines. Physical parameters: $\Xi_{2D} = 0.847$, $\beta = 10$, $\mathrm{Re} = 5.6 \times 10^{-3}$, $\mathrm{Ca} = 8 \times 10^{4}$, and $\mathrm{Bn} = 0$.
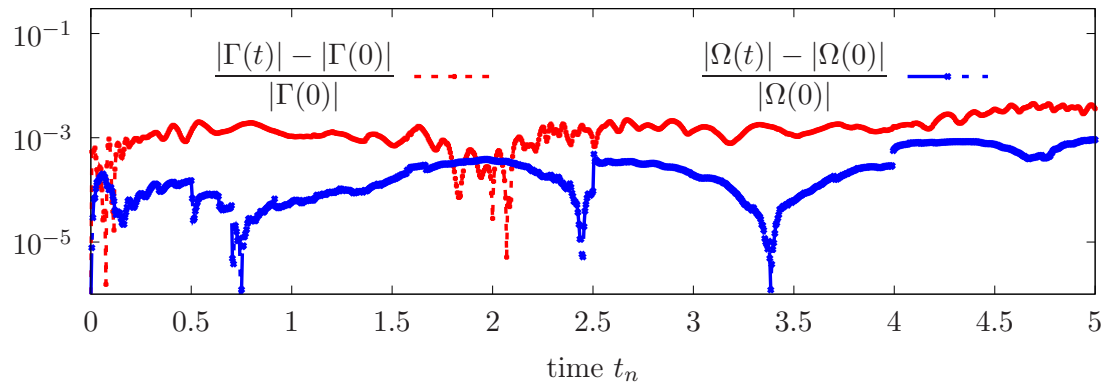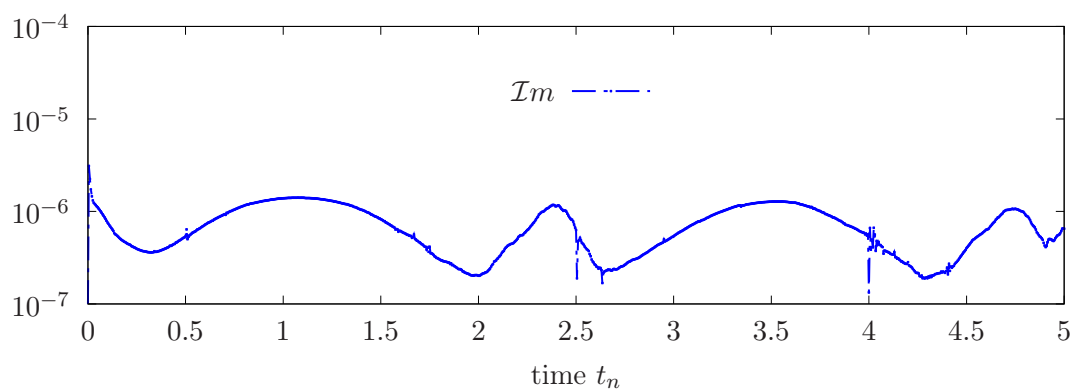
Figure 13. Time evolution of the relative error in the membrane's area and perimeter for a vesicle in a tumbling movement. Logarithmic scale is used on the y axis. Physical parameters: $\Xi_{2D} = 0.847$, $\beta = 10$, $\mathrm{Re} = 5.6 \times 10^{-3}$, $\mathrm{Ca} = 8 \times 10^4$, and $\mathrm{Bn} = 0$.

The angle of inclination of the membrane and the evolution over time of the imaginary part of the solution are provided respectively in Figures 14 and 15. Observe that the imaginary part has four maxima during a tumbling period, which correspond to the angles of the vesicle $0, -\pi/2, -\pi, \pi/2$. In particular, when the angle of inclination is close to $-\pi/2$ and $\pi/2$, the vesicle becomes perpendicular to the flow and undergoes a strong shearing force, inducing better tracking of the latter if the time step is sufficiently small.
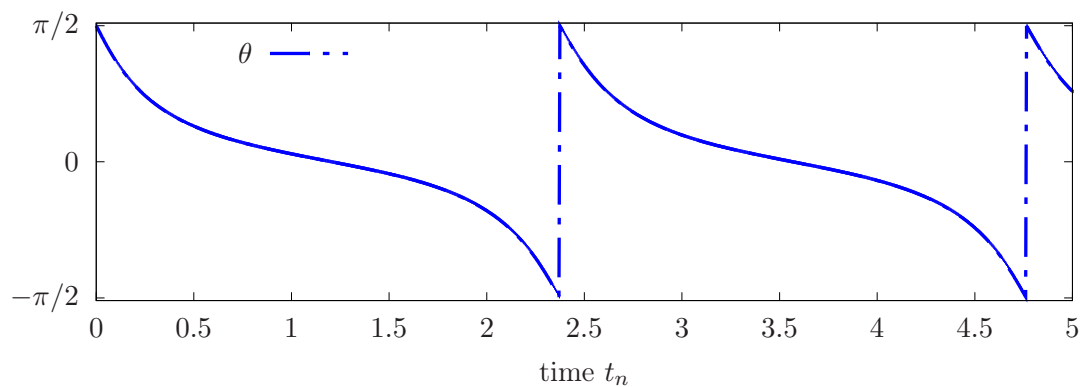
Figure 14. Time evolution of the membrane's inclination angle for a vesicle in a tumbling movement. Physical parameters: $\Xi_{2D} = 0.847$, $\beta = 10$, $\mathrm{Re} = 5.6 \times 10^{-3}$, $\mathrm{Ca} = 8 \times 10^4$, and $\mathrm{Bn} = 0$.

Figure 15. Error estimation based on the imaginary part throughout the simulation period for a vesicle in a tumbling movement. Logarithmic scale is used on the y axis. Physical parameters: $\Xi_{2D} = 0.847$, $\beta = 10$, $\mathrm{Re} = 5.6 \times 10^{-3}$, $\mathrm{Ca} = 8 \times 10^4$, and $\mathrm{Bn} = 0$.

5.2.3. Calibration of the Penalty Parameter

We proceed with a numerical study to better study the setting of the penalty parameter ε_λ. We consider a vesicle with a reduced area $\Xi_{2D} = 0.85$ in simple shear flow and fix a viscosity rate of either $\beta = 1$ (tank-treading motion) or $\beta = 10$ (tumbling motion). The same additional parameters as the previous example are considered. We consider several values of the penalty ε_λ and evaluate in Table 2 the relative error on the perimeter. Errors are calculated over the simulation period as follows:

$$e_{|\Gamma|} = \int_0^T \left| |\Gamma(t)| - |\Gamma(0)| \right| dt.$$

Note that the mass conservation properties are improved by decreasing the penalty parameter, up to a certain value of ε_λ, beyond which the perimeter is less well preserved. Accordingly, we choose $\varepsilon_\lambda = h^{1.5}$ in the following simulations.

Table 2. Evaluation of the relative error on the perimeter of a vesicle with a reduced area $\Xi_{2D} = 0.85$. Sensitivity study of the conservation of the perimeter with respect to the choice of ε_λ. Simulations with a mesh size $h = 1.7 \times 10^{-2}$.

ε_λ	h^1	$h^{1.2}$	$h^{1.4}$	$h^{1.6}$	$h^{1.8}$	h^2	$h^{2.3}$
$\beta = 1$	0.0022	0.021	0.0138	0.0082	0.03692	0.0512	0.0675
$\beta = 10$	0.036	0.0013	0.0027	0.0057	0.0199	0.0309	0.0458

5.2.4. Quantitative Validation with Respect to Existing Results

Subsequently, we proceed to the numerical validation of our method in the Newtonian case with some well-known results in the published literature.

Firstly, we choose the physical parameters $\beta = 1$, Re $= 10^{-3}$, and Ca $= 10^2$. The vesicle follows a tank-treading regime, and we focus on the angle of equilibrium in the steady-state regime. A quantitative validation is performed for different reduced areas $\Xi_{2D} \in [0.6, 0.9]$. Figure 16 shows the steady state inclination angle, denoted by θ^*, obtained with different numerical methods by Laadhari et al. [76], Salac et al. [83], Kraus et al. [88], and Zhao et al. [89], as well as the experimental results provided by Kantsler and Steinberg in [90]. The numerical results show good overall agreement.

Secondly, we set $\beta = 2.7$ and keep the other physical parameters the same. Comparison with the numerical results of Laadhari et al. [76], Zhao et al. [89], and the experimental results in [90] are provided in Figure 17. A satisfactory agreement is observed with regard to the published data.

Finally, we are interested in the transition between tank-treading and tumbling regimes, which occurs at a threshold value of the viscosity ratio, called β^*. This is called the phase diagram. We report in Figure 18 the critical value β^* and compare it with the results obtained from other numerical approaches in [91] (phase-field method, Re = 0), [83] (level-set method, finite difference method), [76] (level-set method, finite element method), Keller and Skalak's theory [92], as well as the experimental results of [90]. A good qualitative and quantitative agreement is observed.

5.3. Example 3: Membrane Dynamics in a Casson Shear Flow

In this test case, we study the effect of the Casson model on the dynamic motion of the membrane.

First, we set $\beta = 1$, Re $= 10^{-3}$, and Ca $= 10^2$. The vesicle then follows a tank-treading motion, and we report the steady-state tilt angle in the case of a purely Newtonian fluid model as well as the change in angle when setting a non-zero Bingham parameter Bn. We consider different reduced areas $\Xi_{2D} \in [0.6, 0.9]$, and we set Casson's regularization $\xi = 10^{-2}$. The results reported in Figure 19 illustrate small changes in tilt angle for small values of Bn, while larger changes are observed for Bn = 2.
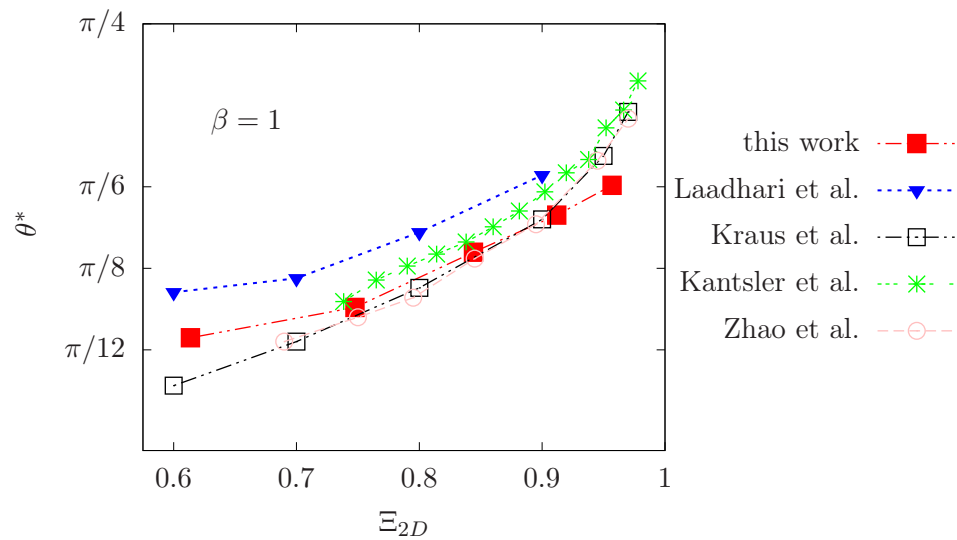
Figure 16. Vesicle under tank-treading regime in simple linear shear flow. Inclination angle at equilibrium θ^* versus the reduced area Ξ_{2D}. Physical parameters: $\beta = 1$, Re $= 10^{-3}$, and Ca $= 10^2$. Comparisons with the published results in Laadhari et al. [76] (Re $= 10^{-3}$ and Ca $= 10^2$), Salac et al. [83] (Re $= 10^{-3}$ and Ca $= 10^2$), Kraus et al. [88] (Ca $= 10$), Zhao et al. [89] (Ca $= 9$), and the experiments of Kantsler and Steinberg [90].
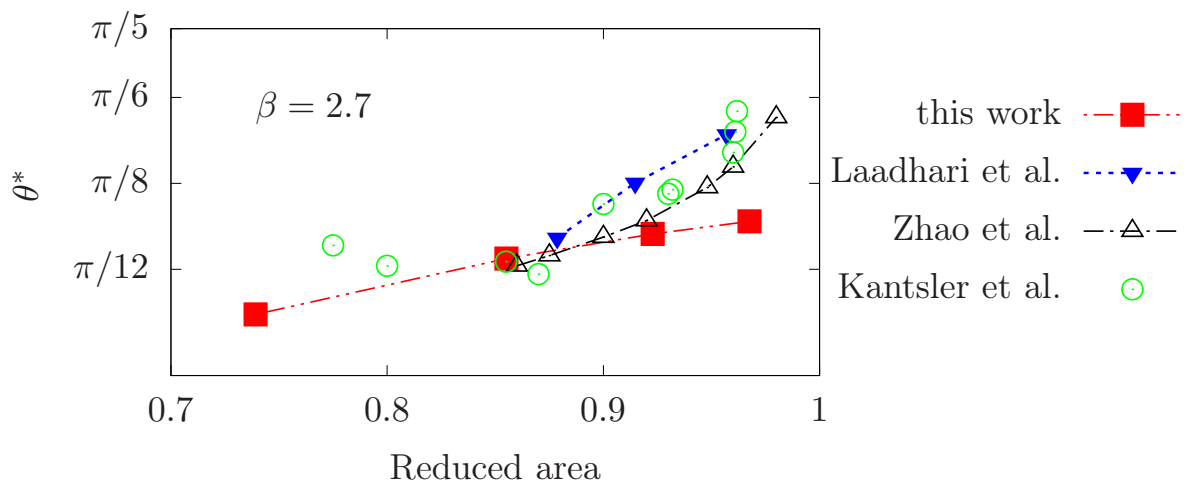

Figure 17. Vesicle following a tank-treading regime in simple linear shear flow. Angle of inclination at equilibrium θ^* with respect to the reduced area Ξ_{2D}. Physical parameters: $\beta = 2.7$, Re $= 10^{-3}$, and Ca $= 10^2$. Comparison with the numerical results published in Laadhari et al. [76], Zhao et al. [89], and the experimental results of Kantsler and Steinberg in [90].

Now, we present a comparative study of the parameters $\beta = 1$, Re $= 10^{-3}$, and Ca $= 10^2$, for both Newtonian and non-Newtonian cases with $Bn = 2$. We observe the motion of a vesicle until it reaches a steady-state regime, undergoing tank-treading. Figure 20 displays the steady-state membrane deformations and the surrounding velocity profile for both cases. Our results indicate that a higher Bingham number leads to an inclination closer to the horizontal position.
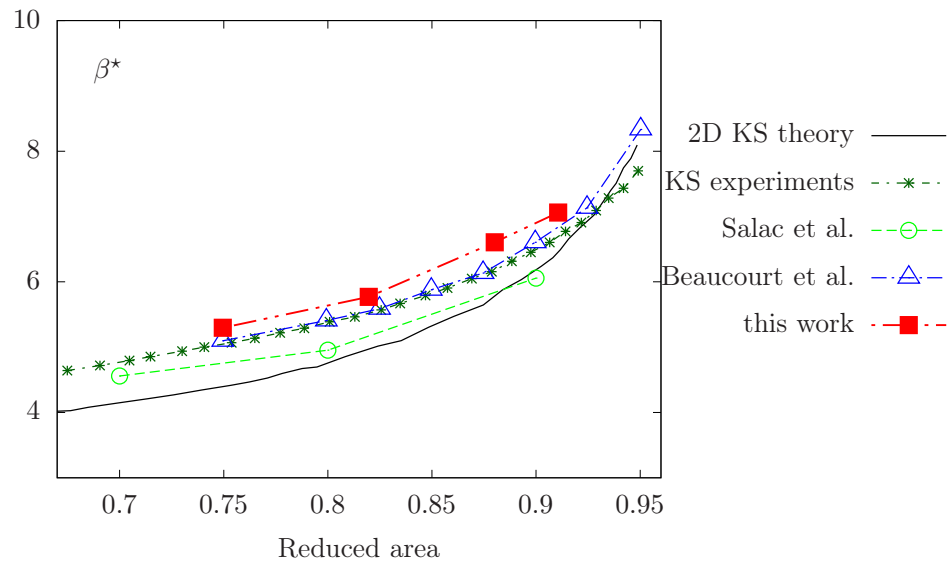
Figure 18. Phase diagram showing the critical viscosity contrast $\beta^\star$ required for the tank-treading/tumbling transition, versus the reduced area parameter Ξ_{2D}. Comparisons with numerical results in [91] (phase-field method, Stokes limit), [83] (level-set, finite difference method), [76] (level-set, finite element method), KS theory [92], and experimental results in [90].
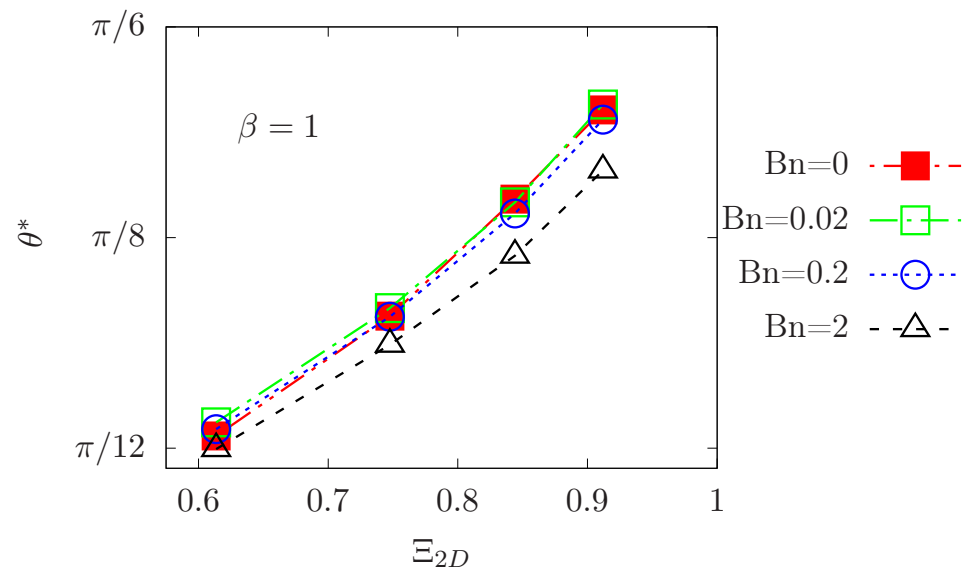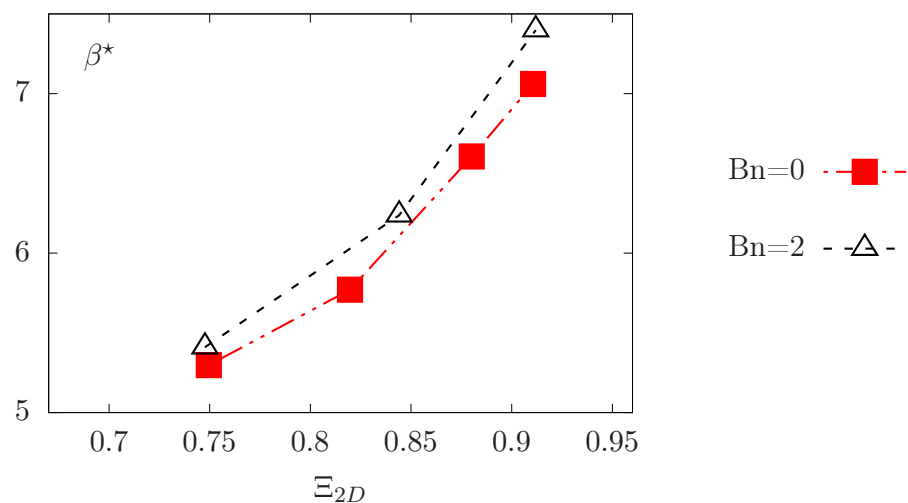

Figure 19. Numerical study of the effect of Casson flow on the vesicle tank-treading motion under simple shear flow conditions. Change in the angle of inclination at equilibrium θ^* with respect to the reduced areas Ξ_{2D} for different values of Bn. Simulation parameters: $\beta = 1$, Re $= 10^{-3}$, and Ca $= 10^2$.

We hereafter study the effect of Casson's rheological model on the phase diagram for Bn $= 2$. The numerical results are reported in Figure 21, showing slightly higher values of the critical viscosity ratio needed to achieve the transition between tank-treading and tumbling regimes.

(**a**)

(**b**)

(**c**)
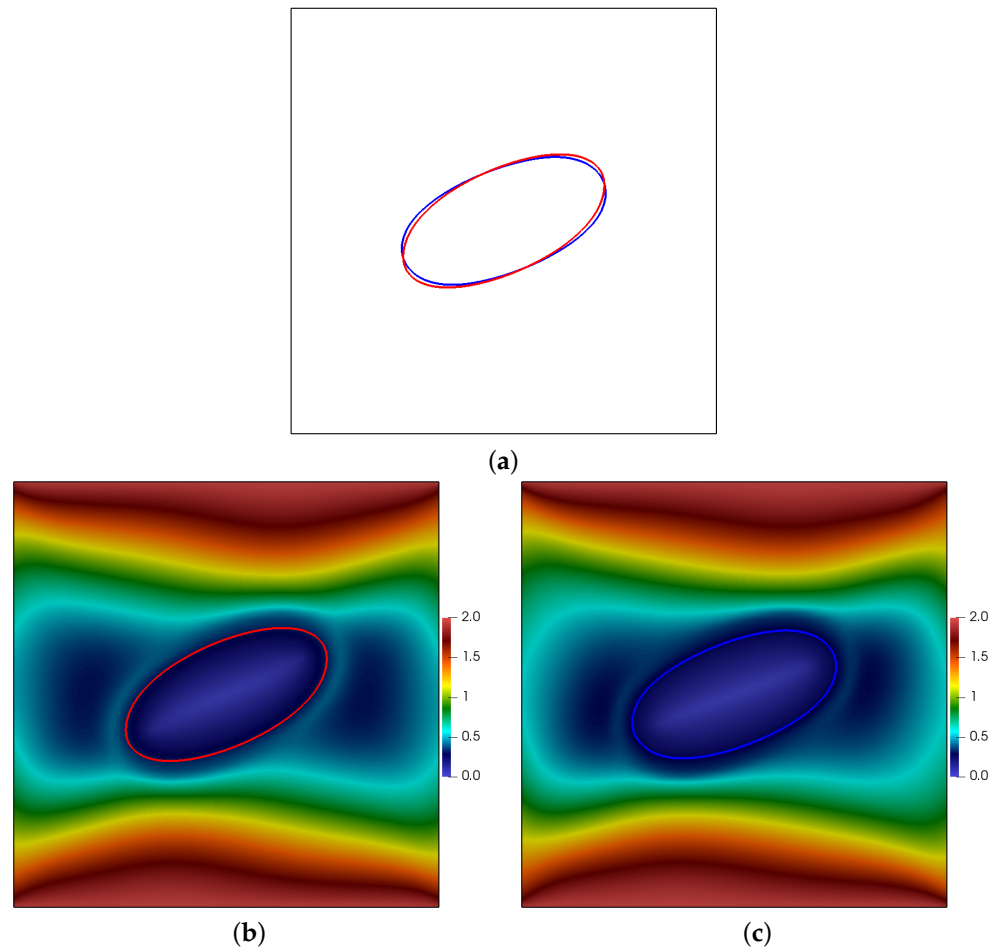
Figure 20. Change in the tank-treading stationary state between the Newtonian and non-Newtonian cases for a vesicle in simple shear flow. (**a**) Bn = 0 (red color), Bn = 2 (blue color). (**b**) Velocity profile for Bn = 0. (**c**) Velocity profile for Bn = 2.

Figure 21. Numerical study of the effect of Casson flow on the transition from tank-treading to tumbling for a vesicle in simple shear flow. Changed critical viscosity contrasts β^* against reduced areas Ξ_{2D} for Bn = 0 and Bn = 2. Physical parameters: Re = 10^{-3} and Ca = 10^2.

In conclusion, Casson's non-Newtonian rheology should have an impact on the dynamics of red blood cells and deserves further efforts to study it. This is beyond the scope of this article, but will be deeply investigated from a biophysical point of view in future work.

6. Conclusions

We introduced a finite element methodology for the numerical simulation of inextensible biomembranes mimicking red blood cells immersed in a non-Newtonian Casson fluid. The main contributions of this article can be summarized as follows: (i) The rheological properties of blood flow in small capillaries are described by a non-Newtonian viscoplastic model through Casson's constitutive law. To our knowledge, this is the first time that a realistic viscoplastic hemorheological model has been considered for the RBC modeling problem. (ii) Our methodology involves the introduction of the numerical integration approach based on the double-flow composition of the basic second-order backward differentiation (BDF-2) formula using complex coefficients in order to increase the order of the method. Our approach allows for an elegant estimation of the error and especially allows us to raise the order of the integrator from 2 to 3. (iii) An adaptive time-stepping strategy is introduced for higher precision in the numerical resolution. The adaptation criterion is based on a precise criterion obtained by projection of the complex approximate solution on the imaginary axis. (iv) Fluid-membrane interactions are handled implicitly through a level-set representation combined with a penalty approach. The method shows good conservation of area and perimeter (crucial issue in Eulerian methods). (v) Several numerical examples involving both ordinary and partial differential equations are performed to assess in detail the relevance of the mathematical model in terms of physiological significance. Convergence analysis is performed, showing the optimal spatio-temporal convergence behaviors. In addition, qualitative and quantitative comparative studies against analytical, numerical, and experimental results known in the published literature are carried out to validate and show the accuracy of the presented numerical approach. (vi) Preliminary study and results for the effect of the non-Newtonian rheological model on RBC regimes under simple shear flow are presented, in the hope of triggering extensive experimental and numerical studies to further explore cellular dynamics in small capillaries.

Some extensions of the developments in this article are currently being explored. In particular, the non-Newtonian effect will be explored in more detail in a separate work. This is part of a larger study of the dynamics of the biological membranes and red blood cells. We focus on developing high-precision mathematical models that better describe the mechanical properties of the cytoskeleton [32,37,93,94]. Motivated by the importance of geometric symmetries in blood flow, we will also study RBC dynamics in realistic three-dimensional axisymmetric geometries as well as flow symmetry. In a predictive modeling framework, we also plan to use the aforementioned algorithms in fluid mechanics learning with the aim of predicting the dynamics of red blood cells. We are also exploring higher-order schemes by composition of symmetric methods of order 2 and multi-step composition for various basic integrators.

Author Contributions: Project administration, A.L.; Funding acquisition, A.L.; Methodology, A.L. and A.D.; Software, A.D.; Writing—review & editing, A.L. and A.D. All authors have read and agreed to the published version of the manuscript.

Data Availability Statement: All data generated during this study are included in this published article.

Conflicts of Interest: The authors declare no conflict of interest.

Appendix A

Note on the Composition Technique for the Level-Set Problem

For the sake of clarity, we provide here some outlines of the numerical implementation of the composition technique applied to solve the level-set advection, that is, to calculate φ_n using the double composition of BDF-2 with complex coefficients. Indeed, we need to perform operations with complex numbers using a mixed formulation and calculate their

real and imaginary parts. To begin with, we introduce the complex field $\Phi \in \mathbb{X} \times \mathbb{X}$ such that $\Phi = \varphi + \mathbf{i}\overline{\varphi}$. It follows that $\varphi = \text{Re}(\Phi)$. A vector notation $\Phi := (\varphi, \varphi)^T$ would be more appropriate and will be adopted. It follows that the internal domain of the membrane is the real part of Φ, that is, $\Omega = \{\mathbf{x} \in \Lambda \text{ s.t. } \varphi(\mathbf{x}) = \text{Re}(\Phi(\mathbf{x})) < 0\}$.

As a consequence, elementary algebraic operations such as addition and multiplication are properly set for arbitrary complex numbers $\Phi^{(1)} = (\varphi^{(1)}, \overline{\varphi}^{(1)})^T$ and $\Phi^{(2)} = (\varphi^{(2)}, \overline{\varphi}^{(2)})^T$ as follows:

$$\Phi^{(1)} + \Phi^{(2)} = \left(\varphi^{(1)} + \varphi^{(2)}, \overline{\varphi}^{(1)} + \overline{\varphi}^{(2)}\right)^T, \tag{A1}$$

$$\Phi^{(1)}\Phi^{(2)} = \left(\varphi^{(1)}\varphi^{(2)} - \overline{\varphi}^{(1)}\overline{\varphi}^{(2)}, \varphi^{(1)}\overline{\varphi}^{(2)} + \overline{\varphi}^{(1)}\varphi^{(2)}\right)^T. \tag{A2}$$

We also define the scalar product in $\mathbb{X} \times \mathbb{X}$, the gradient operator, and the product between tensor elements $\boldsymbol{\nabla}\Phi^{(1)}$ and $\boldsymbol{\nabla}\Phi^{(2)}$ as follows:

$$\left\langle \Phi^{(1)}, \Phi^{(2)} \right\rangle_{\mathbb{X}\times\mathbb{X}} = \left(\left\langle \varphi^{(1)}, \varphi^{(2)} \right\rangle_{\mathbb{X}}, \left\langle \overline{\varphi}^{(1)}, \overline{\varphi}^{(2)} \right\rangle_{\mathbb{X}}\right)^T, \tag{A3}$$

$$\boldsymbol{\nabla}\Phi = (\boldsymbol{\nabla}\varphi, \boldsymbol{\nabla}\overline{\varphi})^T, \tag{A4}$$

$$\left\langle \boldsymbol{\nabla}\Phi^{(1)}, \boldsymbol{\nabla}\Phi^{(2)} \right\rangle_{\mathbb{X}\times\mathbb{X}} = \left(\boldsymbol{\nabla}\varphi^{(1)}\boldsymbol{\nabla}\varphi^{(2)}, \boldsymbol{\nabla}\overline{\varphi}^{(1)}\boldsymbol{\nabla}\overline{\varphi}^{(2)}\right)^T. \tag{A5}$$

Our goal is to find Φ, whose imaginary part will be used to adapt the time step. Starting from a real part corresponding to the level-set function, we set the initial condition $\Phi_0 = (\varphi_0, 0)^T$. The level-set equation is presented in its complex form as follows:

$$\frac{\partial \Phi}{\partial t} + \mathbf{U}.\boldsymbol{\nabla}\Phi = \mathbf{0}. \tag{A6}$$

Here $\mathbf{U} = (\mathbf{u}, \bar{\mathbf{u}})^T$ represents the complex version of the velocity field, with an imaginary part $\bar{\mathbf{u}}$ initially set to zero. For any $n > 1$, the time discretized equation using BDF-2 with variable time steps can be written as follows:

$$\gamma'_2 \Phi_n + \delta t_n \mathbf{U}_n.\boldsymbol{\nabla}\Phi_n = -\left(\gamma'_1 \Phi_{n-1} + \gamma'_0 \Phi_{n-2}\right), \tag{A7}$$

where γ'_i are functions of complex variables representing the coefficients of the BDF-2 scheme with adaptive time steps and δt_n is the time step size.

References

1. Connes, P.; Simmonds, M.J.; Brun, J.F.; Baskurt, O.K. Exercise hemorheology: Classical data, recent findings and unresolved issues. *Clin. Hemorheol. Microcirc.* **2013**, *53*, 187–199. [CrossRef] [PubMed]
2. Fung, Y.C. *Biomechanics*, 2nd ed.; Springer: New York, NY, USA, 1993.
3. Karaz, S.; Senses, E. Liposomes under Shear: Structure, Dynamics, and Drug Delivery Applications. *Adv. NanoBiomed Res.* **1998**, *3*, 2200101. [CrossRef]
4. Thurston, G. Rheological parameters for the viscosity viscoelasticity and thixotropy of blood. *Biorheology* **1979**, *16*, 149–162. [CrossRef] [PubMed]
5. Wajihah, S.A.; Sankar, D. A review on non-Newtonian fluid models for multi-layered blood rheology in constricted arteries. *Arch. Appl. Mech.* **2023**, *93*, 1771–1796. [CrossRef] [PubMed]
6. Chien, S.; Usami, S.; Dellenback, R.; Gregersen, M. Shear-dependent deformation of erythrocytes in rheology of human blood. *Am. J. Physiol.* **1970**, *219*, 136–142. [CrossRef] [PubMed]
7. Merrill, E.E.; Gilliland, E.R.; Cokelet, G.; Shin, H.; Britten, A.; Wells, R.E., Jr. Rheology of human blood, near and at zero flow. Effects of temperature and hematocrit level. *Biophys. J.* **1963**, *3*, 199–213. [CrossRef]
8. Lai, M.C.; Li, Z. A remark on jump conditions for the three-dimensional Navier-Stokes equations involving an immersed moving membrane. *Appl. Math. Lett.* **2001**, *14*, 149–154. [CrossRef]
9. Barrett, J.W.; Garcke, H.; Nurnberg, R. Numerical computations of the dynamics of fluidic membranes and vesicles. *Phys. Rev. E* **2015**, *92*, 052704. [CrossRef]
10. Ayscough, S.E.; Clifton, L.A.; Skoda, M.W.; Titmuss, S. Suspended phospholipid bilayers: A new biological membrane mimetic. *J. Colloid Interface Sci.* **2023**, *633*, 1002–1011. [CrossRef]

11. Noyhouzer, T.; L'Homme, C.; Beaulieu, I.; Mazurkiewicz, S.; Kuss, S.; Kraatz, H.B.; Canesi, S.; Mauzeroll, J. Ferrocene-Modified Phospholipid: An Innovative Precursor for Redox-Triggered Drug Delivery Vesicles Selective to Cancer Cells. *Langmuir* **2016**, *32*, 4169–4178. [CrossRef]

12. Kaoui, B. Computer simulations of drug release from a liposome into the bloodstream. *Eur. Phys. J. E* **2018**, *41*, 20. [CrossRef] [PubMed]

13. Elani, Y.; Law, R.V.; Ces, O. Vesicle-based artificial cells as chemical microreactors with spatially segregated reaction pathways. *Nat. Commun.* **2014**, *5*, 5305. [CrossRef] [PubMed]

14. Seifert, U. Configurations of fluid membranes and vesicles. *Adv. Phys.* **1997**, *46*, 13–137. [CrossRef]

15. Lipowsky, R.; Dimova, R. Introduction to remodeling of biomembranes. *Soft Matter* **2021**, *17*, 214–221. [CrossRef]

16. Helfrich, W. Elastic properties of lipid bilayers: Theory and possible experiments. *Z. Naturforschung C* **1973**, *28*, 693–703. [CrossRef]

17. Canham, P. The minimum energy of bending as a possible explanation of the biconcave shape of the human red blood cell. *J. Theor. Biol.* **1970**, *26*, 61–81. [CrossRef]

18. Bassereau, P.; Sorre, B.; Lévy, A. Bending lipid membranes: Experiments after W. Helfrich's model. *Adv. Colloid Interface Sci.* **2014**, *208*, 47–57. [CrossRef]

19. Zhong-Can, O.Y.; Helfrich, W. Bending energy of vesicle membranes: General expressions for the first, second, and third variation of the shape energy and applications to spheres and cylinders. *Phys. Rev. A* **1989**, *39*, 5280–5288. [CrossRef]

20. Laadhari, A.; Misbah, C.; Saramito, P. On the equilibrium equation for a generalized biological membrane energy by using a shape optimization approach. *Phys. D* **2010**, *239*, 1567–1572. [CrossRef]

21. Kaoui, B.; Ristow, G.H.; Cantat, I.; Misbah, C.; Zimmermann, W. Lateral migration of a two-dimensional vesicle in unbounded Poiseuille flow. *Phys. Rev. E* **2008**, *77*, 021903. [CrossRef]

22. Zhang, T.; Wolgemuth, C.W. A general computational framework for the dynamics of single- and multi-phase vesicles and membranes. *J. Comput. Phys.* **2022**, *450*, 110815. [CrossRef] [PubMed]

23. Zhang, T.; Wolgemuth, C.W. Sixth-Order Accurate Schemes for Reinitialization and Extrapolation in the Level Set Framework. *J. Sci. Comput.* **2020**, *83*, 26. [CrossRef]

24. Bui, C.; Lleras, V.; Pantz, O. Dynamics of red blood cells in 2d. *ESAIM Proc.* **2009**, *28*, 182–194. [CrossRef]

25. Pozrikidis, C. Numerical simulation of the flow-induced deformation of red blood cells. *Ann. Biomed. Eng.* **2003**, *31*, 1194–1205. [CrossRef] [PubMed]

26. Rahimian, A.; Veerapaneni, S.K.; Biros, G. Dynamic simulation of locally inextensible vesicles suspended in an arbitrary two-dimensional domain, a boundary integral method. *J. Comput. Phys.* **2010**, *229*, 6466–6484. [CrossRef]

27. Dodson, W.R.; Dimitrakopoulos, P. Oscillatory tank-treading motion of erythrocytes in shear flows. *Phys. Rev. E* **2011**, *84*, 011913. [CrossRef]

28. Krüger, T.; Varnik, F.; Raabe, D. Efficient and accurate simulations of deformable particles immersed in a fluid using a combined immersed boundary lattice Boltzmann finite element method. *Comput. Math. Appl.* **2011**, *61*, 3485–3505. [CrossRef]

29. Bonito, A.; Nochetto, R.H.; Pauletti, M.S. Parametric FEM for geometric biomembranes. *J. Comput. Phys.* **2010**, *229*, 3171–3188. [CrossRef]

30. Cottet, G.H.; Maitre, E.; Milcent, T. Eulerian formulation and Level-Set models for incompressible fluid-structure interaction. *Math. Model. Numer. Anal.* **2008**, *42*, 471–492. [CrossRef]

31. Laadhari, A.; Saramito, P.; Misbah, C. Computing the dynamics of biomembranes by combining conservative level-set and adaptive finite element methods. *J. Comput. Phys.* **2014**, *263*, 328–352. [CrossRef]

32. Laadhari, A. An operator splitting strategy for fluid-structure interaction problems with thin elastic structures in an incompressible Newtonian flow. *Appl. Math. Lett.* **2018**, *81*, 35–43. [CrossRef]

33. Laadhari, A.; Szekely, G. Fully implicit finite element method for the modeling of free surface flows with surface tension effect. *Int. J. Numer. Methods Eng.* **2017**, *111*, 1047–1074. [CrossRef]

34. Doyeux, V.; Guyot, Y.; Chabannes, V.; Prud'homme, C.; Ismail, M. Simulation of two-fluid flows using a finite element/level-set method. Application to bubbles and vesicle dynamics. *J. Comput. Appl. Math.* **2013**, *246*, 251–259. [CrossRef]

35. Du, Q.; Liu, C.; Wang, X. A phase field approach in the numerical study of the elastic bending energy for vesicle membranes. *J. Comput. Phys.* **2004**, *198*, 450–468. [CrossRef]

36. Valizadeh, N.; Rabczuk, T. Isogeometric analysis of hydrodynamics of vesicles using a monolithic phase-field approach. *Comput. Methods Appl. Mech. Eng.* **2022**, *388*, 114191. [CrossRef]

37. Gera, P.; Salac, D. Modeling of multicomponent three-dimensional vesicles. *Comput. Fluids* **2018**, *172*, 362–383. [CrossRef]

38. Osher, S.; Fedkiw, R.P. Level Set Methods: An Overview and Some Recent Results. *J. Comput. Phys.* **2001**, *169*, 463–502. [CrossRef]

39. Laadhari, A. Implicit finite element methodology for the numerical modeling of incompressible two-fluid flows with moving hyperelastic interface. *Appl. Math. Comput.* **2018**, *333*, 376–400. [CrossRef]

40. Laadhari, A. Exact Newton method with third-order convergence to model the dynamics of bubbles in incompressible flow. *Appl. Math. Lett.* **2017**, *69*, 138–145. [CrossRef]

41. Laadhari, A.; Szekely, G. Eulerian finite element method for the numerical modeling of fluid dynamics of natural and pathological aortic valves. *J. Comput. Appl. Math.* **2017**, *319*, 236–261. [CrossRef]

42. Seol, Y.; Tseng, Y.H.; Kim, Y.; Lai, M.C. An immersed boundary method for simulating Newtonian vesicles in viscoelastic fluid. *J. Comput. Phys.* **2019**, *376*, 1009–1027. [CrossRef]

43. Izbassarov, D.; Muradoglu, M. A front-tracking method for computational modeling of viscoelastic two-phase flow systems. *J. Non-Newton. Fluid Mech.* **2015**, *223*, 122–140. [CrossRef]
44. Suzuki, T.; Takao, H.; Suzuki, T.; Hataoka, S.; Kodama, T.; Aoki, K.; Otani, K.; Ishibashi, T.; Yamamoto, H.; Murayama, Y.; et al. Proposal of hematocrit-based non-Newtonian viscosity model and its significance in intracranial aneurysm blood flow simulation. *J. Non-Newton. Fluid Mech.* **2021**, *290*, 104511. [CrossRef]
45. Gudiño, E.; Oishi, C.M.; Sequeira, A. Influence of non-Newtonian blood flow models on drug deposition in the arterial wall. *J. Non-Newton. Fluid Mech.* **2019**, *274*, 104206. [CrossRef]
46. Blair, G.S. An equation for the flow of blood, plasma and serum through glass capillaries. *Nature* **1959**, *183*, 613–614. [CrossRef] [PubMed]
47. Merrill, E.W.; Pelletier, G.A. Viscosity of human blood: Transition from Newtonian to non-Newtonian. *J. Appl. Physiol.* **1967**, *23*, 178–182. [CrossRef]
48. Charm, S.; Kurland, G. Viscometry of human blood for shear rates of 0–100,000 $\sec^{-1}$. *Nature* **1965**, *206*, 617–618. [CrossRef] [PubMed]
49. Casson, N. A Flow Equation for Pigment-oil Suspensions of the Printing Ink Type. In *Rheology of Disperse Systems*; Mills, C.C., Ed.; Pergamon Press: Oxford, UK, 1959; pp. 84–104.
50. Fasano, A.; Sequeira, A. *Hemomath*, 1st ed.; Springer: Cham, Switzerland, 2017. [CrossRef]
51. Papanastasiou, T.C. Flows of Materials with Yield. *J. Rheol.* **1987**, *31*, 385–404. [CrossRef]
52. Fusi, L.; Calusi, B.; Farina, A.; Rosso, F. Stability of laminar viscoplastic flows down an inclined open channel. *Eur. J. Mech. B/Fluids* **2022**, *95*, 137–147. [CrossRef]
53. Shahzad, H.; Wang, X.; Ghaffari, A.; Iqbal, K.; Hafeez, M.B.; Krawczuk, M.; Wojnicz, W. Fluid structure interaction study of non-Newtonian Casson fluid in a bifurcated channel having stenosis with elastic walls. *Sci. Rep.* **2022**, *12*, 12219. [CrossRef]
54. Aghighi, M.S.; Ammar, A.; Metivier, C.; Gharagozlu, M. Rayleigh-Bénard convection of Casson fluids. *Int. J. Therm. Sci.* **2018**, *127*, 79–90. [CrossRef]
55. Hairer, E.; Lubich, C.; Wanner, G. *Geometric Numerical Integration: Structure-Preserving Algorithms for Ordinary Differential Equations*; Springer Series in Computational Mathematics; Springer: Berlin/Heidelberg, Germany, 2002.
56. Hairer, E.; Lubich, C.; Wanner, G. Geometric numerical integration illustrated by the Störmer–Verlet method. *Acta Numer.* **2003**, *12*, 399–450. [CrossRef]
57. Leimkuhler, B.; Reich, S. *Simulating Hamiltonian Dynamics*; Cambridge Monographs on Applied and Computational Mathematics; Cambridge University Press: Cambridge, UK, 2005. [CrossRef]
58. Cromer, A.H. Stable solutions using the Euler approximation. *Am. J. Phys.* **1981**, *49*, 455–459. [CrossRef]
59. Yoshida, H. Construction of higher order symplectic integrators. *Phys. Lett. A* **1990**, *150*, 262–268. [CrossRef]
60. McLachlan, R.I. On the Numerical Integration of Ordinary Differential Equations by Symmetric Composition Methods. *SIAM J. Sci. Comput.* **1995**, *16*, 151–168. [CrossRef]
61. Blanes, S.; Casas, F.; Murua, A. Splitting and composition methods in the numerical integration of differential equations. *Bol. Scc. Esp. Mat. Apl.* **2008**, *45*, 89–145.
62. Blanes, S.; Casas, F. *A Concise Introduction to Geometric Numerical Integration*, 1st ed.; Chapman and Hall/CRC: Boca Raton, FL, USA, 2016. [CrossRef]
63. Casas, F.; Chartier, P.; Escorihuela-Tomàs, A.; Zhang, Y. Compositions of pseudo-symmetric integrators with complex coefficients for the numerical integration of differential equations. *J. Comput. Appl. Math.* **2021**, *381*, 113006. [CrossRef]
64. Bickart, T.; Picel, Z. High order stiffly stable composite multistep methods for numerical integration of stiff differential equations. *BIT Numer. Math.* **1973**, *13*, 272–286. [CrossRef]
65. Channell, P.J. Hybrid symplectic integrators for relativistic particles in electric and magnetic fields. *Comput. Sci. Discov.* **2014**, *7*, 015001. [CrossRef]
66. Senyange, B.; Skokos, C. Computational efficiency of symplectic integration schemes: Application to multidimensional disordered Klein–Gordon lattices. *Eur. Phys. J. Spec. Top.* **2018**, *227*, 625–643. [CrossRef]
67. Bader, P.; Blanes, S.; Casas, F.; Kopylov, N. Novel symplectic integrators for the Klein–Gordon equation with space- and time-dependent mass. *J. Comput. Appl. Math.* **2019**, *350*, 130–138. [CrossRef]
68. Blanes, S.; Casas, F.; Farrés, A.; Laskar, J.; Makazaga, J.; Murua, A. New families of symplectic splitting methods for numerical integration in dynamical astronomy. *Appl. Numer. Math.* **2013**, *68*, 58–72. [CrossRef]
69. Butusov, D.N.; Andreev, V.S.; Pesterev, D.O. Composition semi-implicit methods for chaotic problems simulation. In Proceedings of the 2016 XIX IEEE International Conference on Soft Computing and Measurements (SCM), St. Petersburg, Russia, 25–27 May 2016; pp. 107–110. [CrossRef]
70. Deeb, A.; Razafindralandy, D.; Hamdouni, A. Performance of Borel-Padé-Laplace integrator for the solution of stiff and non-stiff problems. *Appl. Math. Comput.* **2022**, *426*, 127118. [CrossRef]
71. Deeb, A.; Razafindralandy, D.; Hamdouni, A. Comparison between Borel-Padé summation and factorial series, as time integration methods. *Discrete Contin. Dyn. Syst. Ser. S* **2016**, *9*, 393–408. [CrossRef]
72. Hairer, E.; Nørsett, S.P.; Wanner, G. *Solving Ordinary Differential Equations I: Nonstiff Problems*, 2nd ed.; Springer Series in Computational Mathematics Vol 1; Springer: Berlin/Heidelberg, Germany, 2009.

73. Sunday, J.; Shokri, A.; Kwanamu, J.A.; Nonlaopon, K. Numerical Integration of Stiff Differential Systems Using Non-Fixed Step-Size Strategy. *Symmetry* **2022**, *14*, 1575. [CrossRef]
74. Evans, E.A. Bending Resistance and Chemically Induced Moments in Membrane Bilayers. *Biophys. J.* **1974**, *14*, 923–931. [CrossRef]
75. Deuling, H.; Helfrich, W. Red blood cell shapes as explained on the basis of curvature elasticity. *Biophys. J.* **1976**, *16*, 861–868. [CrossRef] [PubMed]
76. Laadhari, A.; Saramito, P.; Misbah, C.; Székely, G. Fully implicit methodology for the dynamics of biomembranes and capillary interfaces by combining the Level Set and Newton methods. *J. Comput. Phys.* **2017**, *343*, 271–299. [CrossRef]
77. Shibeshi, S.S.; Collins, W.E. The Rheology of Blood Flow in a Branched Arterial System. *Appl. Rheol.* **2005**, *15*, 398–405. [CrossRef]
78. Calusi, B.; Farina, A.; Fusi, L.; Rosso, F. Long-wave instability of a regularized Bingham flow down an incline. *Phys. Fluids* **2022**, *34*, 137–147. [CrossRef]
79. Suzuki, M. Fractal decomposition of exponential operators with applications to many-body theories and Monte Carlo simulations. *Phys. Lett. A* **1990**, *146*, 319–323. [CrossRef]
80. Iserles, A. *A First Course in the Numerical Analysis of Differential Equations*, 2nd ed.; Cambridge University Press: Cambridge, UK, 2008.
81. Donelson, J., III; Hansen, E. Cyclic Composite Multistep Predictor-Corrector Methods. *SIAM J. Numer. Anal.* **1971**, *8*, 137–157. [CrossRef]
82. Tendler, J.M.; Bickart, T.A.; Picel, Z. A stiffly stable integration process using cyclic composite methods. *ACM Trans. Math. Softw.* **1978**, *4*, 339–368. [CrossRef]
83. Salac, D.; Miksis, M. Reynolds number effects on lipid vesicles. *J. Fluid Mech.* **2012**, *711*, 122–146. [CrossRef]
84. Janela, J.; Lefebvre, A.; Maury, B. A penalty method for the simulation of fluid—Rigid body interaction. *ESAIM Proc.* **2005**, *14*, 115–123. [CrossRef]
85. Brooks, A.N.; Hughes, T.J. Streamline upwind/Petrov–Galerkin formulations for convection dominated flows with particular emphasis on the incompressible Navier-Stokes equations. *Comput. Methods Appl. Mech. Eng.* **1982**, *32*, 199–259. [CrossRef]
86. Loch, E. The Level Set Method for Capturing Interfaces with Applications in Two-Phase Flow Problems. Ph.D. Thesis, Aachen University, Aachen, Germany, 2013.
87. Alnaes, M.; Blechta, J.; Hake, J.; Johansson, A.; Kehlet, B.; Logg, A.; Richardson, C.; Ring, J.; Rognes, M.E.; Wells, G.N. The FEniCS Project Version 1.5. *Arch. Numer. Softw.* **2015**, *3*, 9–23.
88. Kraus, M.; Wintz, W.; Seifert, U.; Lipowsky, R. Fluid vesicles in shear flow. *Phys. Rev. Lett.* **1996**, *77*, 3685. [CrossRef]
89. Zhao, H.; Shaqfeh, E.S.G. The dynamics of a vesicle in simple shear flow. *J. Fluid Mech.* **2011**, *674*, 578–604. [CrossRef]
90. Kantsler, V.; Steinberg, V. Transition to Tumbling and Two Regimes of Tumbling Motion of a Vesicle in Shear Flow. *Phys. Rev. Lett.* **2006**, *96*, 036001. [CrossRef]
91. Beaucourt, J.; Rioual, F.; Séon, T.; Biben, T.; Misbah, C. Steady to unsteady dynamics of a vesicle in a flow. *Phys. Rev. E* **2004**, *69*, 011906. [CrossRef] [PubMed]
92. Keller, S.R.; Skalak, R. Motion of a tank-treading ellipsoidal particle in a shear flow. *J. Fluid Mech.* **1982**, *120*, 27–47. [CrossRef]
93. Laadhari, A.; Barral, Y.; Székely, G. A data-driven optimal control method for endoplasmic reticulum membrane compartmentalization in budding yeast cells. In *Mathematical Methods in the Applied Sciences*; Wiley Online Library: Hoboken, NJ, USA, 2023. [CrossRef]
94. Gizzi, A.; Ruiz-Baier, R.; Rossi, S.; Laadhari, A.; Cherubini, C.; Filippi, S. A Three-dimensional Continuum Model of Active Contraction in Single Cardiomyocytes. In *Modeling the Heart and the Circulatory System*; Springer International Publishing: Cham, Switzerland, 2015; pp. 157–176. [CrossRef]